In vitro integration of a functional vasculature to model endothelial regulation of chemotherapy and T-cell immunotherapy in liver cancer

Jyothsna Vasudevan[1], Ragavi Vijayakumar[2], Jose Antonio Reales-Calderon[2], Maxine S Y Lam[2], Jin Rong Ow[2], Joey Aw[2], Damien Tan[2], Anthony Tanoto Tan[3], Antonio Bertoletti[3], Giulia Adriani[4,5] and Andrea Pavesi[1,2,6*]

[1]Jyothsna Vasudevan, Andrea Pavesi
Mechanobiology Institute, National University of Singapore (NUS), 5A Engineering Drive 1, Singapore 117411, Republic of Singapore.
[*]Corresponding author: andreap@imcb.a-star.edu.sg

[2]Ragavi Vijayakumar, Jose Antonio Reales-Calderon, Maxine S Y Lam, Jin Rong Ow, Joey Aw, Damien Tan, Andrea Pavesi
Institute of Molecular and Cell Biology (IMCB), Agency for Science, Technology and Research (A*STAR), 61 Biopolis Drive, Singapore 138673, Republic of Singapore.

[3]Anthony Tanoto Tan, Antonio Bertoletti
Duke-NUS Medical School, 8 College Road, Singapore 169857, Republic of Singapore.

[4]Giulia Adriani
Singapore Immunology Network (SIgN), Agency for Science, Technology, and Research (A*STAR), 8A Biomedical Grove, Immunos, Singapore 138648, Republic of Singapore.
[5]Department of Biomedical Engineering, National University of Singapore (NUS), 4 Engineering Drive 3, Singapore 117583, Republic of Singapore.

[6]Andrea Pavesi
Lee Kong Chian School of Medicine (LKCMedicine), Nanyang Technological University, Singapore 308232

Graphical abstract

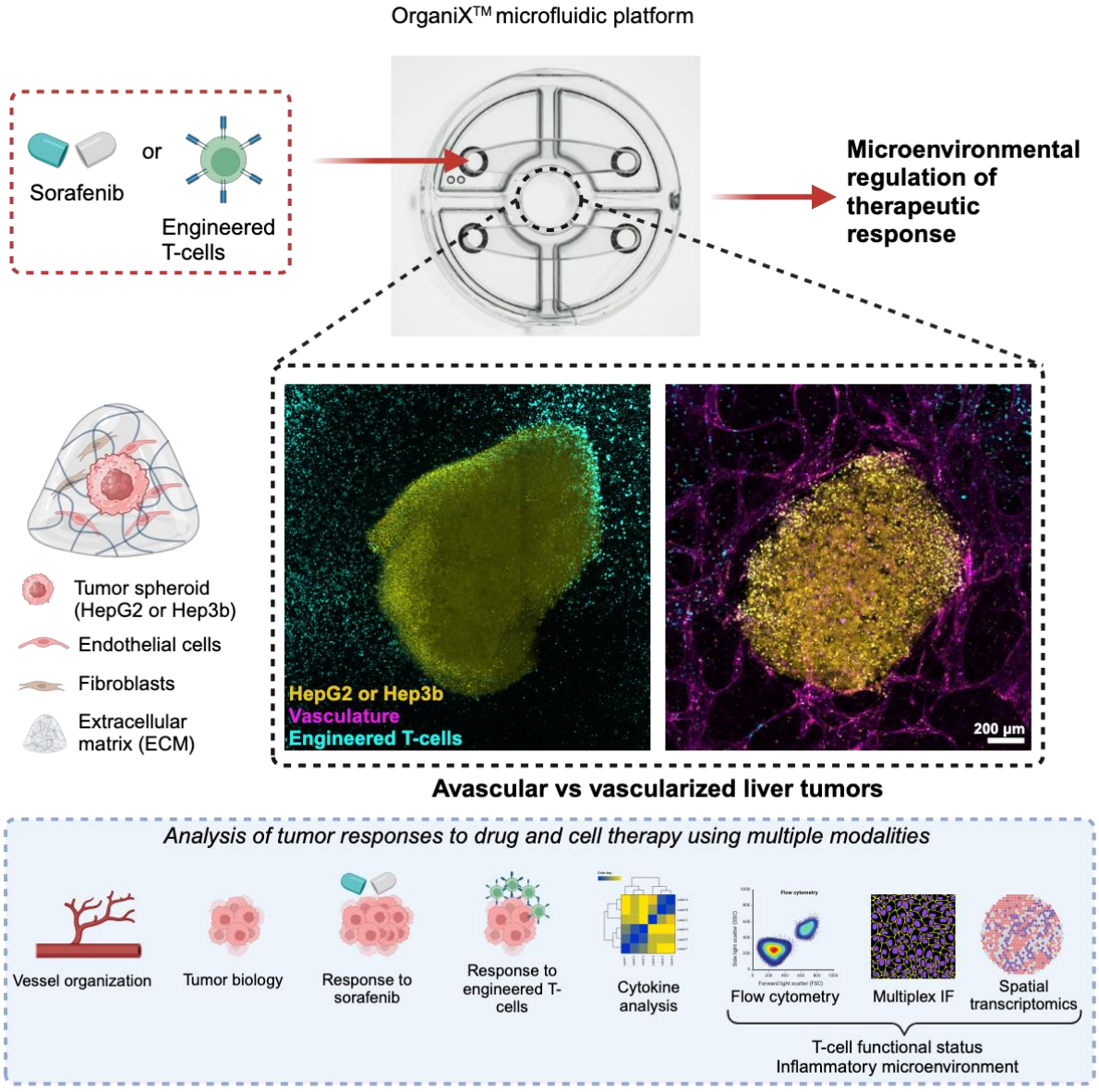

Abstract

The complex tumor microenvironment (TME) presents significant challenges to the development of effective therapies against solid tumors, highlighting the need for advanced *in vitro* models that better recapitulate TME biology. To address this, we developed a vascularized human liver tumor model using a microfluidic platform, designed to test both drug and cell-based therapies. This model mimics critical tumorigenic features such as hypoxia, extracellular matrix (ECM), and perfusable vascular networks. Intravascular administration of Sorafenib demonstrated its ability to disrupt vascular structures significantly, while eliciting heterogeneous responses in two distinct liver tumor cell lines, HepG2 and Hep3b. Furthermore, treatment with engineered T-cells revealed that the tumor vasculature impeded T-cell infiltration into the tumor core but preserved their cytotoxic capacity, albeit with reduced exhaustion levels. Cytokine analysis and spatial profiling of vascularized tumor samples identified proinflammatory factors that may enhance T-cell-mediated antitumor responses. By capturing key TME characteristics, this microfluidic platform provides a powerful tool enabling detailed investigation of tumor-immune and tumor-vascular interactions. Its versatility could serve as a promising bridge between preclinical studies and clinical testing, offering opportunities for developing and optimizing personalized therapeutic strategies for solid tumors.

Keywords

Liver cancer, tumor microenvironment, chemotherapy, immunotherapy, microfluidics

Introduction

Hepatocellular carcinoma (HCC) accounts for 70% of liver cancer diagnoses globally and is the sixth leading cause of cancer-related deaths[1, 2]. Patients diagnosed at an early stage are eligible for surgical resection, local ablation, or liver transplantation[3]. However, most patients present with advanced-stage disease, necessitating chemotherapy[4-7]. Acquired resistance to these standard drug treatments is often inevitable, driving the need for a new standard of care for refractory tumors[8, 9]. In the last few decades, cancer management has undergone a revolutionary transformation through the advent of immunotherapy. Adoptive cell therapy using chimeric antigen receptor T-cells (CAR-T) and receptor-modified T-cells (TCR-T) has shown preliminary efficacy in phase I/II clinical trials[10-13]. Although these innovative therapies have obvious scientific promise, successful clinical translation is far from certain as obstacles within the solid tumor microenvironment (TME), such as tissue fibrosis, inflammatory milieu, hypoxia, and tumor-associated vasculature, often alter the performance of these engineered T-cells.

The TME serves as a multifaceted canvas that regulates the interactions between tumors and other surrounding cell types. The intricate composition of the HCC TME includes endothelial cells, tumor cells, immune cells, and fibroblasts, forming a dynamic ecosystem within the native extracellular matrix (ECM) that influences therapeutic responses[14]. Signaling molecules are released in response to cell-cell and cell-ECM interactions, driving tumor cells to evade immune surveillance. The uncontrolled proliferation of tumor cells results in the development of a hypoxic TME, which subsequently drives tumor angiogenesis[15, 16]. Tumor-associated vasculature controls the infiltration of effector T-cells into inflammatory sites to rapidly execute cytolysis[17, 18]. Therefore, recognizing the significance of the impact of TME stressors on T-cells is crucial for enhancing adoptive cell therapy and improving the survival rates of patients with HCC.

Two-dimensional (2D) cultures inadequately represent numerous aspects of the TME, including 3D tissue architecture, cellular heterogeneity and polarity, and gradients of soluble factors, such as nutrients, cytokines, and oxygen[19]. Three-dimensional (3D) microphysiological organotypic models, or organ-on-chips, have been developed to overcome these limitations in recapitulating TME features and enable the observation of the dynamics of tumor-stroma interactions. These platforms offer a controlled environment to dissect the role of specific cues in tumor response, overcoming the inherent complexity of *in vivo* models. Recent studies have designed microphysiological models to assess and improve the effectiveness of immunotherapies, including immune checkpoint inhibitors, adoptive cell therapy, and epigenetic inhibitors[20, 21]. In particular, vascularized tumor models are promising for examining heterotypic cellular interactions related to disease progression and for therapeutic screening[22, 23]. Recently, we have seen great research efforts toward developing vascularized tumor models for drug screening[24-26] and immune cell responses[27-31], thereby highlighting the significance of investigating TME modulation of therapeutic strategies with direct clinical implications. However, to the best of our knowledge, the specific role of the tumor-associated vasculature in altering drug response and immune cell effector functions within the HCC tumor microenvironment remains elusive, thereby highlighting the need for further investigation.

Here, we introduce a microphysiological system designed for culturing and vascularizing HCC spheroids (HepG2 and Hep3b) within a 3D fibrin-collagen matrix to assess drug responses and engineered T-cell therapeutic efficacy in the presence or absence of vasculature. We aimed to

recapitulate key features of the HCC tumor microenvironment (TME), including (1) a hypoxic tumor core, (2) a tumorigenic extracellular matrix (ECM) niche, and (3) perfusable vascular networks. We tested the efficacy of Sorafenib in this tumor model to heterogeneity in drug responses between the tumor variants. Finally, we expanded the capabilities of our model by incorporating two distinct types of engineered T cells: TCR-T (T-cell receptor therapy)) cells and CAR-T (chimeric antigen receptor T-cell therapy) cells. This allowed us to investigate the complex interplay between engineered T cells and the tumor vasculature. Our findings confirmed the dual role of the vasculature in both enhancing and suppressing T cell effector functions, highlighting the importance of considering the tumor microenvironment in the development of T cell-based therapies.

Results

Microphysiological models of liver tumor integrating a functional vasculature

In this study, we utilized a commercially available microfluidic platform (OrganiX^{TM}, AIM Biotech) to construct a microphysiological model of vascularized liver tumors (Fig. 1A). Two types of liver tumors were used to form spheroids: (i) HBV-infected liver cancer with HepG2-PreS1-GFP (HepG2), expressing the HBV envelope protein linked to GFP, which is targeted by TCR+T cells[12, 13] and (ii) Hep3b, characterized by high endogenous levels of CD133, which is targeted by CD133+ CAR-T cells[10, 32]. The dimensions of spheroids generated using the hanging drop technique were carefully optimized by varying the number of cells in the initial cell suspension. The diameters were ensured to be greater than 500 μm to recapitulate a hypoxic core (Fig. S1). Spheroids were mixed in a collagen and fibrin solution and injected into the central gel region of OrganiX to form an ECM-mimicking hydrogel. Each tumor spheroid was cultured either alone or in combination with human umbilical vein endothelial cells (HUVECs) and normal human lung fibroblasts (NHLF) at a ratio of 4:1, which self-assembled into a vascular network. Vascularized spheroids of both liver tumor cell lines were formed within 7 days of co-culture.

A qualitative assessment of vessel perfusability using 70 kDa fluorescently labeled dextran and time-lapse confocal imaging revealed that the fluorescent probes penetrated efficiently, reaching the tumor periphery within 30 min (Fig. 1B). Quantification of the permeability coefficients of vessels surrounding both the HepG2 and Hep3b tumor spheroids yielded values in the range of 1.6-1.9 × 10^{-7} cm/s (Fig. 1C). Vasculature coverage over time was measured as a percentage of the area of the vasculature in four different regions of interest (ROI) (Fig. 1D): (1) over the entire ROI excluding the tumor area (referred to as the ECM region), (2) at the proximal (<300 μm from the spheroid center), (3) distal (>300-1000 μm from the spheroid center) regions of the spheroid, and (4) within the whole tumor spheroid (TS) region. In the ECM region, the vasculature coverage around HepG2 was 20.19 ± 2.88%, and for Hep3b spheroids, it was 10.21 ± 4.86% (Fig. 1E). Over time, we observed that the coverage values increased and peaked by day 4, remaining almost constant afterward for both liver tumor variants. By day 7, no significant differences in vasculature coverage were observed in the ECM regions of HepG2 and Hep3b spheroids. The initial difference in coverage could be due to the variability in seeding or differences in the distribution of HUVECs and nHLFs within the ECM region. In-depth analysis to assess the localized effects of the tumor spheroid on the vasculature showed that the Hep3b spheroids possessed a significantly higher vasculature coverage at proximal regions than at distal regions (Fig. 1F). In contrast, HepG2 spheroids presented lower vasculature coverage in proximal regions than in distal regions. Furthermore,

the vasculature was observed to penetrate more significantly into Hep3b spheroids (Fig. 1G). In HepG2 tumors, vessels were mainly organized around the periphery of the spheroid. Quantification of vasculature coverage within Hep3b (11.89 ± 1.76%) spheroids was significantly higher in comparison to the HepG2 (3.68 ± 3.15%) spheroids (Fig. 1H), thereby confirming our observations from the images. We also observed the lumen diameters of vessels surrounding the Hep3b spheroids were significantly larger (85.91 ± 25.81 μm) compared to those surrounding HepG2 spheroids (58.11 ± 20.58 μm) (Fig. S2). Overall, our model demonstrated how the organization of tumor-associated vasculature can vary within distinct liver tumor subtypes. With a greater capacity to attract endothelial cells and, subsequently, promote matrix remodeling, Hep3b tumors may more closely resemble the *in vivo* characteristics of human liver tumors than HepG2 tumors.

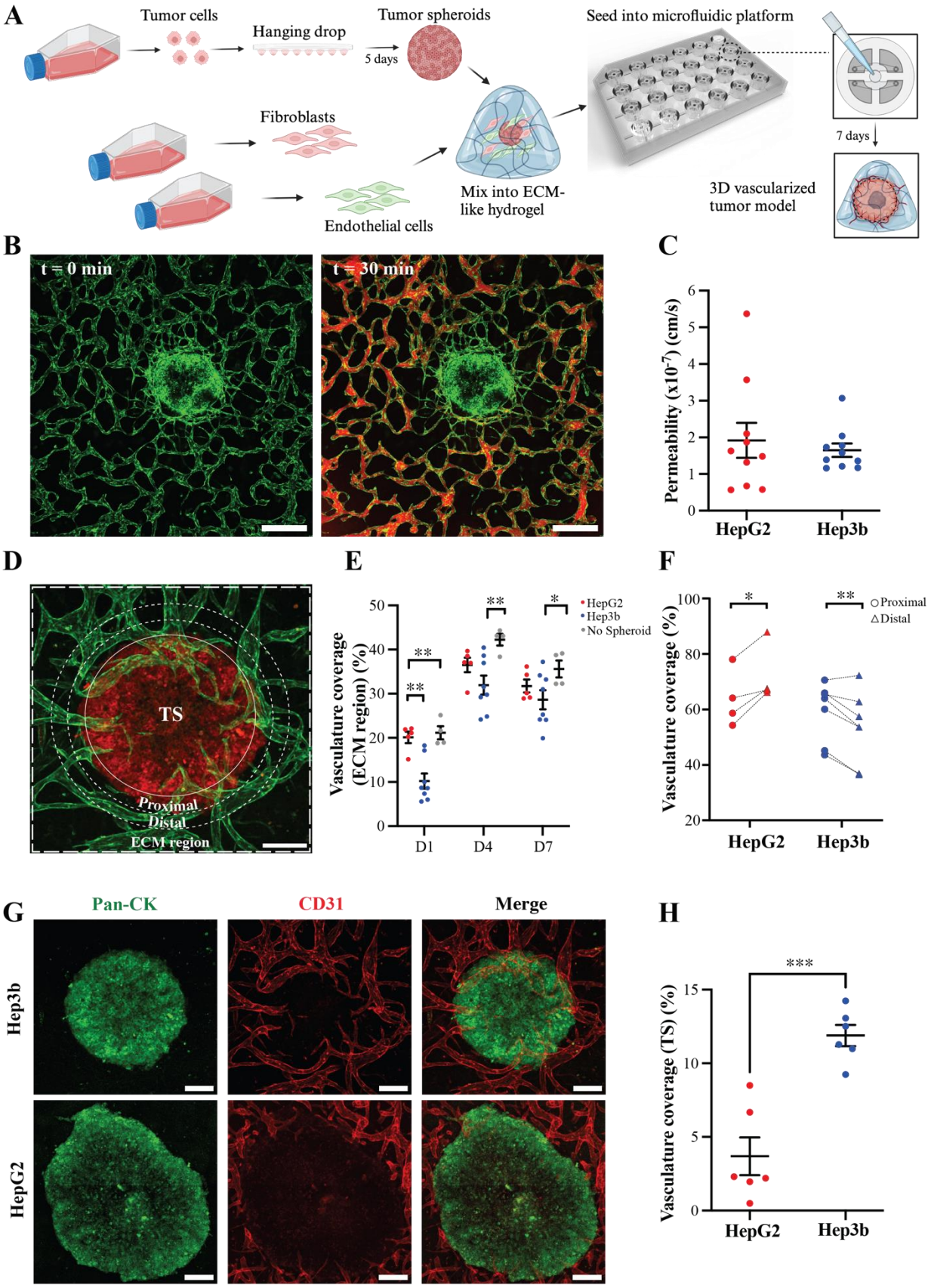

Fig. 1: Microphysiological system with vascularized HCC spheroids. (A) Schematic representation of the workflow for the development of a 3D in vitro vascularized tumor model. HCC cells were cultured in hanging

drops to form HCC tumor spheroids. The spheroids, HUVECs, and NHLFs were suspended in a collagen-fibrin solution and injected into the middle region of the microfluidic device flanked by two lateral fluidic channels containing cell culture media. HUVECs and NHLFs self-assembled to form a vascular network around the HCC spheroids to perfuse media, drugs, and cells; (B) Representative confocal images at different time points after perfusion of the vascularized Hep3b spheroids with 70 kDa fluorescently labeled dextran. Scale bar = 500 µm; (C) Quantification of permeability coefficients of 70 kDa dextran perfused within vascularized tumor models developed with Hep3b (blue) and HepG2 (red) spheroids; (D) Image representation of various regions under consideration for analysis of vasculature coverage. Scale bar = 200 µm. The area (%) of the GFP signal was quantified within the tumor spheroid (TS), proximal (<500 µm from the spheroid edge), distal (500-1000 µm from the spheroid edge), and ECM region, total area of the ROI of the image excluding the spheroid area; (E) Vasculature coverage (%) over time in the ECM region. X-axis represents time in days ('D'); (F) Proximal and distal analysis of the vasculature coverage in Hep3b (in blue) and HepG2 (in red) spheroids; (G) Immunofluorescence staining of spheroids for markers, Pan-CK (green) and CD31 (red). Scale bar = 200 µm; (H) Quantification of vasculature coverage within the tumor spheroid (TS) region. Data are presented as mean ± standard error of the mean (SEM) of n independent replicates, $n \geq 3$. Statistical significance was determined using Student's t-test with a confidence level of $\alpha = 0.05$. * = $p \leq 0.05$, ** = $p \leq 0.01$, *** = $p \leq 0.001$, **** = $p \leq 0.0001$.

Vasculature penetration into tumor spheroids alters intratumoral hypoxia levels

Next, we investigated the impact of tumor-endothelial interactions on various tumor characteristics such as size, proliferation, apoptosis, and hypoxia (Fig. 2A)**.** Spheroid sizes were observed and quantified on day 7 of culture, relative to day 1. In both HepG2 and Hep3b tumor spheroids, vascular networks did not significantly alter the relative tumor area (Fig. 2B, C). We further assessed changes in tumor characteristics such as proliferation, apoptosis and intratumoral hypoxia (Fig. 2D). Vascularized tumors were observed to have highly proliferative cells in comparison to their avascular counterparts (Fig. 2E). No significant differences in caspase-3 levels were observed between vascularized and avascular tumors (Fig. 2E). HIF1α staining demonstrated a notable decline in hypoxia levels within vascularized Hep3b and HepG2 spheroids compared to their non-vascularized tumors (Fig. 2F). In summary, we showed that our experimental platform can be used to reveal alterations in tumor properties based on microenvironmental composition.

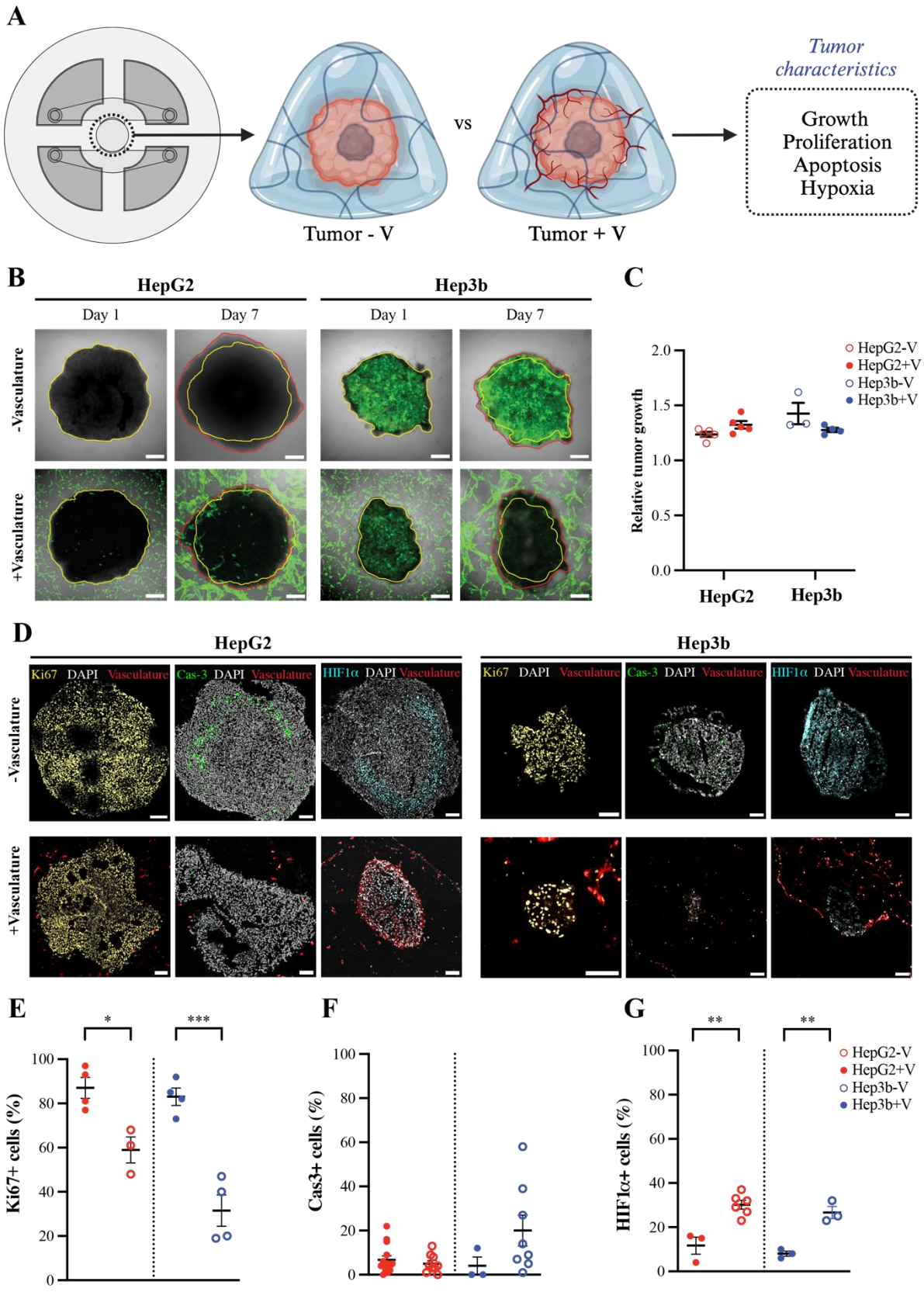

215
216
217
218
219

Fig. 2: Effect of the Vasculature on HCC tumor characteristics. (A) Schematic representation of the parameters used to characterize the effect of vasculature on tumor spheroid. (B) Changes in tumor size in the presence or absence of vasculature. The yellow line represents tumor size measured 1 day post seeding in the device, and the red line indicates the change in tumor area 7 days post seeding. Scale bar = 200 μm; (C) Quantification of relative tumor growth (area of tumor at day 7/area of tumor at day 1) based on measurements from (B); (D) Vascularized and avascular HepG2 and Hep3b tumor cryosections (10 μm thickness) stained for Ki67 (yellow), Caspase-3 (blue) and HIF1α (cyan). Nuclei were labelled with DAPI (white/gray) and the vasculature was visualized using the GFP channel (red). Scale bar = 100 μm; Quantification of (E) Ki67+ (%), (F) cleaved caspase-3+ (Cas3+) (%) and (G) Hif1α+ (%) cells within the tumor region. Data represented as mean ± SEM of n independent replicates where $n \geq 3$. Statistical significance was determined by Student t-test with a confidence level $\alpha = 0.05$. * = $p \leq 0.05$, ** = $p \leq 0.01$, *** = $p \leq 0.001$, **** = $p \leq 0.0001$.

Impact of Tumor Vascularization on Chemotherapy Efficacy

Sorafenib is a multi-target tyrosine kinase inhibitor that is commonly administered as first-line therapy for patients with advanced HCC owing to its antiangiogenic and antiproliferative effects[4, 33]. It suppresses the proliferation of tumor cells by inhibiting Raf-1 kinase in the RAS/RAF/MEK/ERK signaling pathway[34]. It also reduces tumor vascularization and vascular endothelial growth factor (VEGF) production by inhibiting HIF-1α protein production[35]. Substantial data and clinical experience support sorafenib as the mainstay treatment for HCC.

We treated vascularized HCC models with sorafenib to evaluate the effect of vascular networks on drug delivery and antitumor efficacy (Fig. 3A). Before incorporating the drugs into our microphysiological system, cells were first seeded in 2D monolayers or 3D spheroids in a 96 well plate. Post seeding, cells were treated with varying sorafenib concentrations for 48 hr to evaluate the IC_{50} values (Fig 3B). In the 2D configuration, the IC_{50} values established from the dose-response curves for HepG2 and Hep3b were 11.65 μM and 14.66 μM, respectively. Meanwhile, in the 3D configuration, the IC_{50} values increased to 16.65 μM and 20.03 μM, respectively, suggesting that spheroids in the 3D configuration have a greater resistance to the drugs than cells cultured in 2D substrates.

Next, we treated vascularized and avascular HepG2 and Hep3b spheroids with 20 μM sorafenib for 48 h (Fig. 3C, D). Cell death over time was quantified as the percentage area (%area) of DRAQ7 fluorescence in tumor spheroids. Our investigation into the effects of sorafenib treatment on tumor spheroids revealed a complex interplay between vascularization and drug efficacy. After 2 days of drug treatment, the vasculature surrounding the HepG2 tumors was significantly disrupted (Fig. 3C). Quantification of overall tumor death showed that the drug induced higher death in avascular HepG2 spheroids than in their vascularized counterparts (Fig. S3A). When we specifically analyzed the tumor core (~200 μm from the center) (Fig. 3E), vascularized spheroids showed higher tumor death than avascular tumors. This suggests that while the presence of vasculature may initially provide a protective effect against sorafenib, it ultimately facilitates more effective drug penetration and cytotoxicity within the tumor core over time.

Similar to the trends observed in HepG2 cells, the overall tumor death in avascular Hep3b tumors was higher than that in vascularized Hep3bs (Fig. S3B). After 2 days of sorafenib treatment, the vessels were significantly disrupted. The majority of dead cells were observed around the periphery of the tumor. Notably, the tumor core of the vascularized microtissues remained highly treatment-resistant, as indicated by the significantly lower number of dead cells within the core region (Fig. 3F). These results demonstrate the versatility of our

experimental platform, which successfully enabled the evaluation of differential responses to sorafenib across various subtypes of liver tumors.

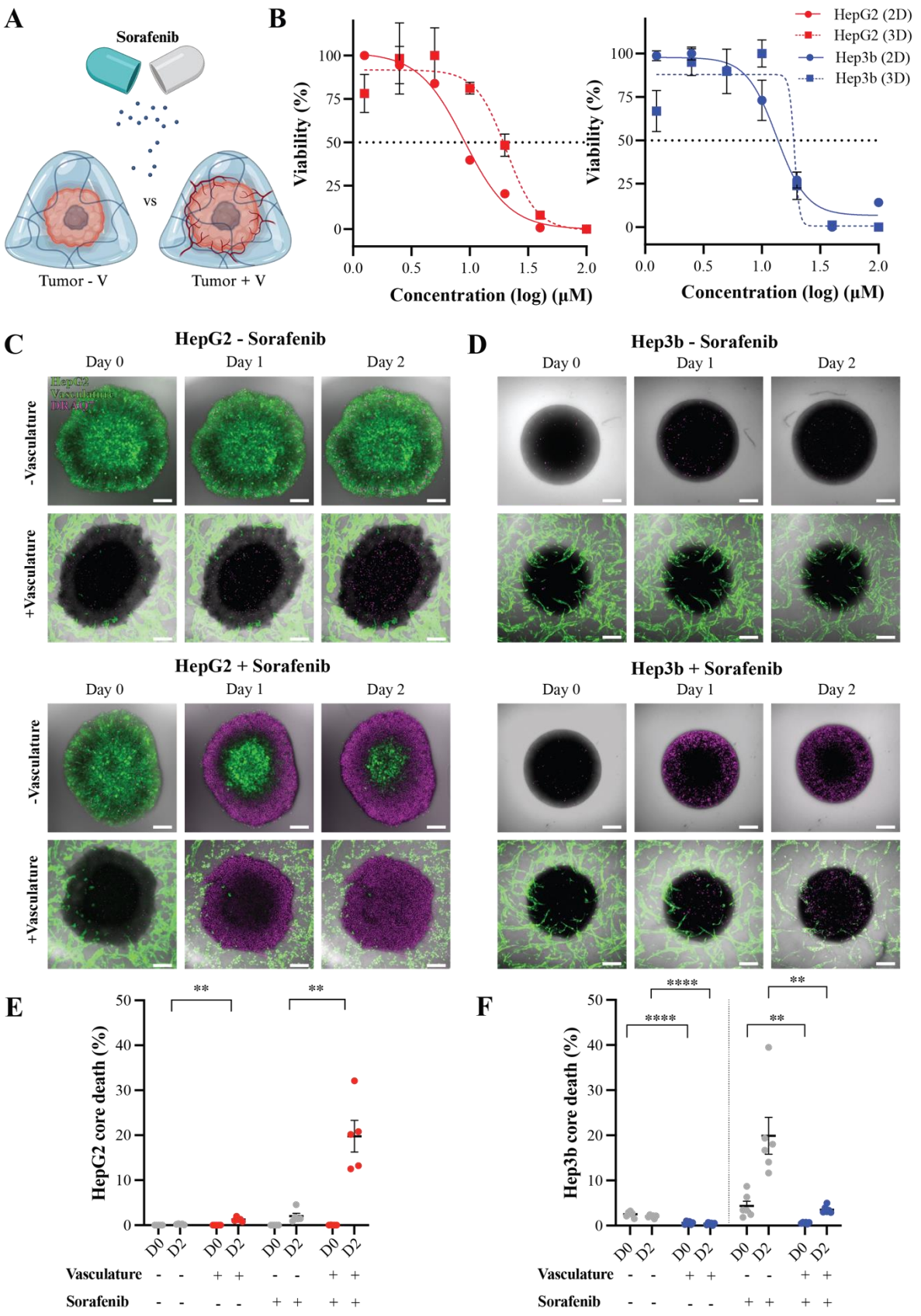

Fig. 3: Effect of Tumor Vascularization on Sorafenib Efficacy. (A) Tumor spheroids +/- vasculature were treated with sorafenib 7 days post seeding in the device; (B) IC_{50} dose-response curve for Hep3b and HepG2 as 2D single cells and 3D spheroids seeded in a 96 well plate with increasing concentrations of sorafenib. The concentration curves were recorded after 24 h of treatment; (C) Brightfield and fluorescence images of

vascularized and avascular HepG2 spheroids seeded in the device treated (i) without (control) and (ii) with sorafenib; (D) brightfield and fluorescence images of vascularized and avascular Hep3b spheroids seeded in the device treated (i) without (control) and (ii) with sorafenib; (E) quantification of cell death within the core region (200 μm from the center) of HepG2 spheroids based on DRAQ7 (magenta) signal from (C). Tumor death within the core measured over time in days ('D'); (F) quantification of cell death within the core region (200 μm from the center) of Hep3b spheroids based on DRAQ7 (magenta) signal from (D). Tumor death within the core measured over time in days ('D'). Data are represented as the mean ± SEM of n independent replicates where n ≥ 3. Lines over bars indicate that the conditions were significantly different, as determined by Student's t-test with $\alpha = 0.05$ (*$p \leq 0.05$, **$p \leq 0.01$, ***$p \leq 0.001$, ****$p \leq 0.0001$).

Evaluation of engineered T-cell infiltration and cytotoxic capacity in the *in vitro* tumor platform

Developing an effective cancer immunotherapy strategy requires a thorough understanding of how T-cell functions are regulated via cellular interactions and the pathological milieu. In this context, we examined two distinct adoptive cell therapy approaches: (1) CD133-specific chimeric antigen receptor (CAR)-modified T-cell therapy and (2) transient expression of T-cell receptor (TCR) T-cell therapy.

Peripheral blood mononuclear cells (PBMCs) from healthy donors were used to isolate T-cells, which were subsequently subjected to retroviral transduction of a CAR construct that expressed a red fluorescence protein (RFP). The transduction efficiency of our protocol yielded approximately 20% CD133-specific CAR-T cells, which were isolated by fluorescence-activated cell sorting (FACS). Gating was performed based on the RFP signal co-expressed with CD133 construct (Fig. S4A, B). The cytotoxic effects of T-cells on Hep3b were first assessed in 2D cultures using xCELLigence® real-time cell analysis. T cells from four different donors were used in the experiments to account for donor variability. Compared with untransduced and non-specific T-cells, engineered CD133+ CAR-T cells were highly effective in targeting Hep3b cells (Fig. S4C). It should be noted that experiments with CD133+ CAR-T cells were not conducted using HepG2 cells because of the absence of CD133 expression (Fig. S6A).

Next, we assessed the infiltration and cytotoxic capacity of CD133+ CAR-T cells using our *in vitro* liver tumor platform (Fig. 4A). We introduced CD133+ CAR-T cells, along with the DRAQ7 fluorescent dye, into the side channels of the microfluidic platform 7 days after seeding the tumor-stromal cell mixture and forming the vasculature. We co-cultured CAR-T cells with vascularized and avascular Hep3b tumors for 6 days and analyzed the levels of infiltration and cytotoxicity. The 3D reconstructed views of CD133+CAR T-cells infiltrating the tumor is shown in Fig S5. Imaging of the DRAQ7 signal revealed that avascular tumors accumulated dead cell populations in both the periphery and center of the tumor region. In contrast, dead cells accumulated mainly in the periphery of the vascularized Hep3b tumors (Fig. 4B). CAR-T cells penetrated the tumor core in avascular spheroids (Fig. 4C), with most cells accumulating in the peripheral region. However, vascularized tumors had a relatively lower number of T-cells, with very few CAR-T cells penetrating the tumor core. Quantitative assessment of DRAQ7 signal (Fig. 4D) indicated an increase in the number of dead cells over time, with avascular tumors showing significantly higher tumor death than vascularized spheroids. Interestingly, while the number of CAR-T cells increased over time in avascular Hep3bs, vascularized tumors showed no significant difference in CAR-T cell numbers (Fig. 4E). Further assessment of tumor death relative to the number of infiltrating CAR-T cells revealed significantly higher tumor death in vascularized spheroids than that in spheroids without vasculature (Fig. 4F). This shows that despite low infiltration levels, it is possible for

T-cell effector functions to be maintained despite encountering the physical barrier formed by the tumor endothelium.

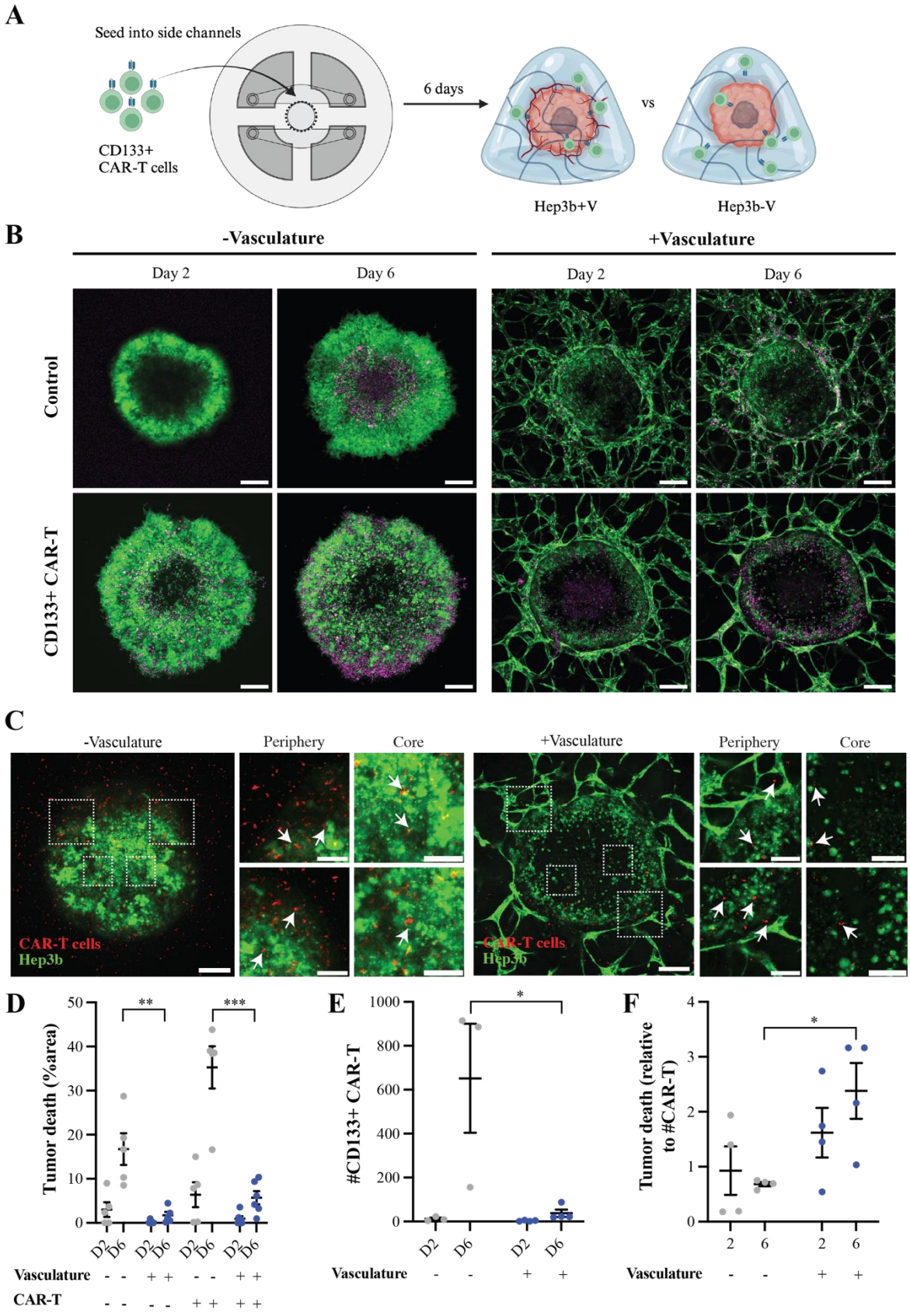

Fig. 4: (A) Schematic showing assessment of CD133+ CAR-T cells on tumor responses; (B) Representative images of vascularized and avascular Hep3b (Green) tumors in the presence/absence of CD133+ CAR-T cells. Images were taken on days 2 and 6 post-coculture and monitored for the number of dead cells accumulated over time, as indicated by the DRAQ7 (magenta) signal. Scale bar = 200 μm; (C) Images showing CD133+ CAR-T cells (red) infiltrating the vascularized and avascular Hep3b (green) tumors on day 6. Scale bar = 200 μm; (D) Quantification of tumor death (%area) within the tumor region using DRAQ7 signal (magenta) from images in (B); (E) Quantification of the number of infiltrating CD133+ CAR-T cells within the tumor spheroids from images in (C); (F) Tumor death relative to the number of CD133+ CAR-T cells. This was calculated as the ratio of the DRAQ7 signal accumulated over time to the number of CD133+ CAR-T cells. Data represented as the mean ± SEM of n independent replicates, $n \geq 3$. Statistical significance was determined by Student t-test with a confidence level $\alpha = 0.05$. * = $p \leq 0.05$, ** = $p \leq 0.01$, *** = $p \leq 0.001$, **** = $p \leq 0.0001$.

Transient-engineered TCR+T cells were generated via mRNA transfection to express a specific TCR recognizing the complex HLA-A0201 molecule and the hepatitis B Env183-191 epitope. In patients, the use of HBV-engineered T-cells carries the risk of T-cells being unable to differentiate between HBV-infected hepatocytes and tumor cells, which can exacerbate hepatitis [12, 13]. As the mRNA HBV TCR-T cells temporarily express the introduced HBV-TCRs[20], their functional duration can be restricted, thereby mitigating any inflammation triggered by the treatment.

We assessed the TCR+T cell mediated HepG2 cytotoxicity in our 3D model after 18 h of treatment (Fig. 5A). This time point was chosen based on the loss of TCR expression at 24 h post-electroporation (Fig. S6B). T-cells from four different donors were used in the experiments to account for donor variability. Compared with untransduced and non-specific T-cells, engineered TCR+T cells were highly effective in targeting HepG2 cells cultured in 2D (Fig. S6C). The 3D reconstructed views of TCR+T-cells infiltrating the tumor is shown in Fig S7. Avascular tumors experienced significantly more tumor death than vascularized HepG2 spheroids (Fig. 5B, D). The presence of an endothelial barrier lowered the number of infiltrating T-cells in the tumor region (Fig. 5C, E). Tumor death relative to the number of TCR+T cells was insignificant compared to that in avascular tumors (Fig. 5F). Our platform successfully captured differences in tumor responses to adoptive cell therapy based on the approaches taken to engineer T-cells.

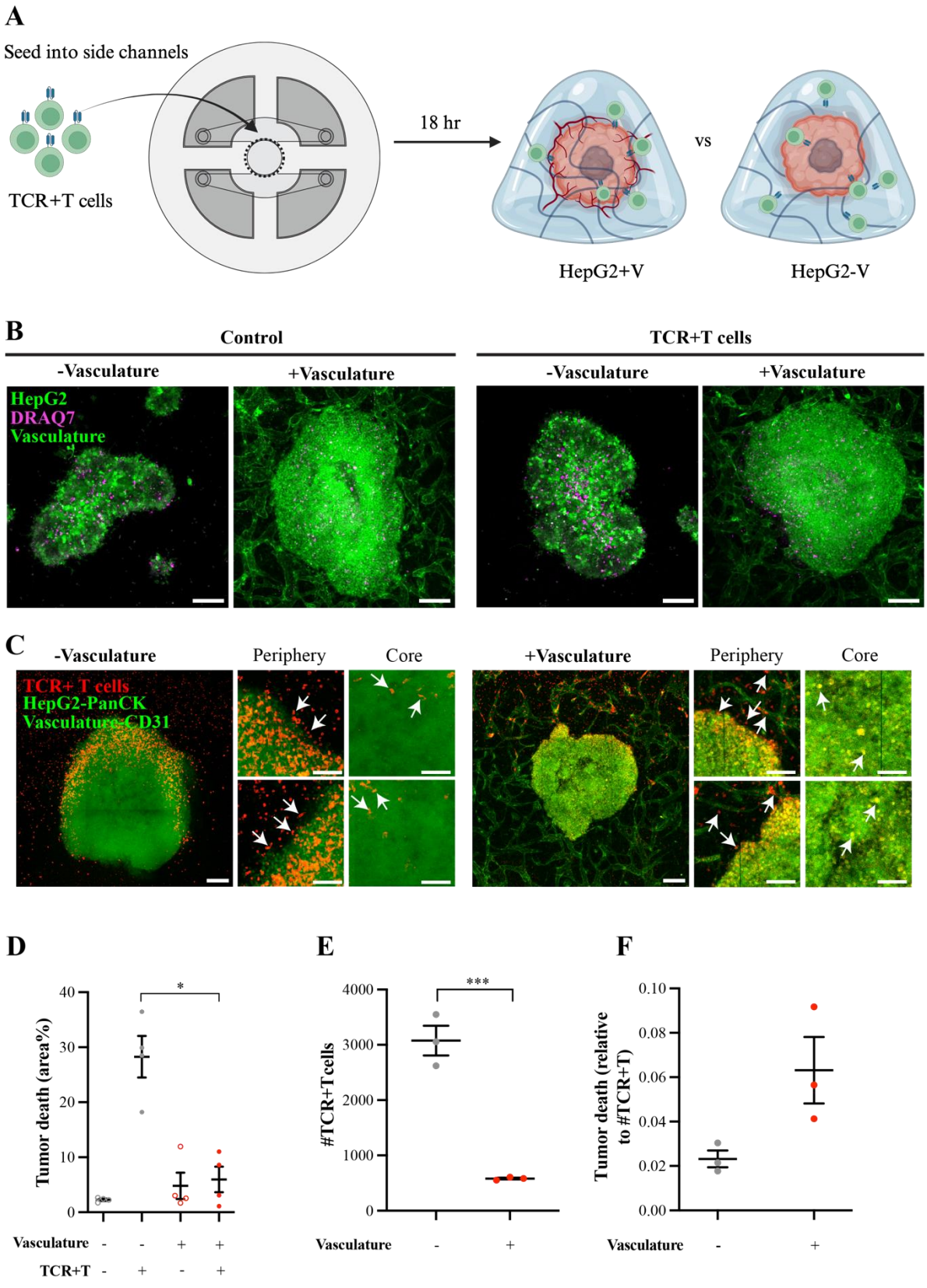

Fig. 5: (A) Schematic showing assessment of TCR+T cells on tumor responses; (B) Representative images of vascularized and avascular HepG2 tumors in the presence or absence of TCR+T cells. Images were taken at 18 hrs post coculture. Tumor spheroids were monitored for the number of dead cells accumulated over time, as

indicated by the DRAQ7 (magenta) signal. Scale bar = 200 μm; Immunofluorescence staining was performed using markers, PanCK (green, tumor region) and CD31 (green, vasculature region); (C) Images showing TCR+T cells (red) infiltrating the vascularized and avascular HepG2 (green) tumors after 18 hrs. Scale bar = 200 μm; (D) Quantification of tumor death (%area) within the tumor region using DRAQ7 signal (magenta) from images in (B); (E) Quantification of the number of infiltrating TCR+T cells within the tumor spheroids from images in (C); (F) Tumor death relative to the number of TCR+T cells. This was calculated as the ratio of the DRAQ7 signal accumulated over time to the number of TCR+T cells. Data represented as the mean ± SEM of n independent replicates, $n \geq 3$. Statistical significance was determined by Student t-test with a confidence level $\alpha = 0.05$. * = $p \leq 0.05$, ** = $p \leq 0.01$, *** = $p \leq 0.001$, **** = $p \leq 0.0001$.

Impact of tumor vasculature on T cell activation and exhaustion status

Next, we performed flow cytometry analysis to understand the changes in the functional status of T-cells that transmigrated into the tumor region through an endothelial monolayer (Fig. 6A). Tumor cells were seeded in the central gel compartment of the iDenTx platform (AIM Biotech). Endothelial cells were seeded onto the side channels and incubated at 37°C to allow for monolayer formation. Subsequently, CAR-T cells were introduced into the side channels and co-cultured with the tumor cells within this platform for 2 days. The infiltrated T-cells within the gel region and those within the side channels were individually isolated and profiled for activation and exhaustion characteristics by flow cytometry. The gating strategy adopted to characterize T-cells has been illustrated in Fig S8.

The presence of an endothelial monolayer resulted in the enhancement of the T cell activation marker cluster of differentiation 25 (CD25) but did not affect the major histocompatibility complex, class II alpha (HLA-DR) (Fig. 6B, C). The endothelium caused a significant reduction in lymphocyte activating gene (LAG-3) and programmed cell death protein-1 (PD-1), but did not significantly affect T-cell immunoglobulin and mucin domain (TIM-3). In contrast, T-cells migrating into the tumor region without passing through the endothelium showed a significantly higher expression of exhaustion markers (LAG-3 and PD-1) (Fig. 6D, E). T-cells from both vascularized and avascular Hep3b devices produced similar levels of cytolytic factors: interferon gamma (IFNγ), granzyme B (GznB) and tumor necrosis factor alpha (TNFα) (Fig 6F). The extracted T-cells were also profiled for memory characteristics (Fig 6G): effector memory (T_{EM}) (CCR7- CD45RO+), central memory (CCR7+ CD45RO+), naïve T (CCR7+ CD45RO-) and effector memory T-cells re-expressing CD45RA (CCR7- CD45RO-). Phenotypic analysis indicated a predominance of TEMRA population, with no marked differences in the %TEMRA T-cells cultured in vascularized and avascular Hep3b devices. These data suggest that the tumor endothelium may play a role in reducing the exhaustion levels of CD133+ CAR-T cells that transmigrated into the inflammatory tumor tissue.

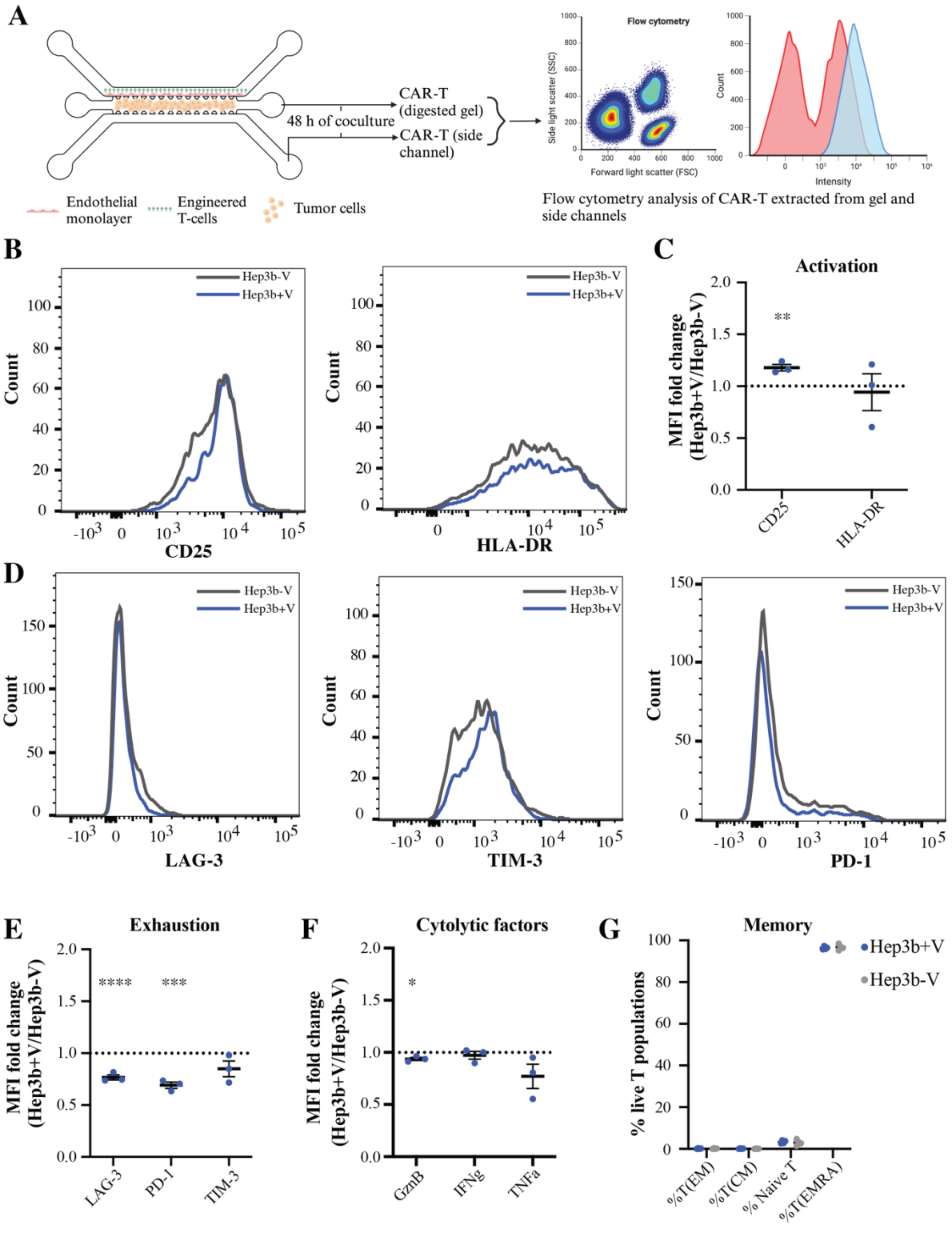

Fig. 6: Flow cytometric analysis of CAR-T cells cocultured with vascularized and avascular Hep3b tumors. (A) Schematic representation of experimental workflow. CAR-T cells were incorporated into the microfluidic device 7 days post vessel formation. The devices were cultured for 48 h. CAR-Ts from the side channels were first collected followed by enzymatic digestion of the central gel region to obtain the encapsulated CAR-T cells for flow cytometric analysis; (B) Flow cytometry evaluation of activation markers, CD25 and HLA-DR; (C) Mean

fluorescence intensity (MFI) of T-cell activation markers from digested tumor microtissues; (D) Flow cytometry evaluation of exhaustion markers; (E) MFI of T-cell exhaustion markers exhaustion markers from digested tumor microtissues; (F) Flow profiling of T cell cytolytic factor production: IGNγ, TNFα and GznB; (G) Evaluation of memory subtypes from digested vascularized and avascular tumor microtissues; Data represented as the mean ± SEM of n independent replicates, $n \geq 3$. Statistical significance was determined by Student t-test with a confidence level $\alpha = 0.05$. * = $p \leq 0.05$, ** = $p \leq 0.01$, *** = $p \leq 0.001$, **** = $p \leq 0.0001$.

Cytokine profiling within the TME

Conditioned media from the devices before sorafenib and T-cell treatment was collected and assessed for soluble factors using a multiplex bead-based immune assay (Luminex). Principal component analysis (PCA) (Fig. 7A) showed that vascularized and avascular HepG2 cells were more closely correlated, as indicated by the low angle between the vectors. Conversely, vascularized and avascular Hep3b cells exhibited distinct separation. The intimate interaction between Hep3b tumors and the surrounding vasculature may induce noteworthy changes in tumor features, consequently leading to a diminished correlation between vascularized and avascular Hep3b tumors. Unsupervised hierarchical clustering separated the vascularized and avascular samples, resulting in two distinct analyte groups (Fig. 7B). We observed that vascularized tumors have lower-than-average secretion levels of pro-angiogenic cytokines like EGF, VEGF, and FGF-2 as opposed to the secretion levels in avascular tumors. During angiogenesis, stromal cells consume pro-angiogenic factors like VEGF and EGF to build and maintain new vessels. This consumption could lead to lower detectable levels of these factors in the surrounding media. Compared to avascular Hep3b tumors, vascularized tumors were observed to have increased levels of proinflammatory cytokines IL-6, IL-8, and CXCL-10, and cytokines that promote T-cell differentiation, such as IL-15 (Fig. 7C). This shows that the cells from the vascularized tumor niche drain secreted factors that could help maintain T-cell activation status within the microenvironment.

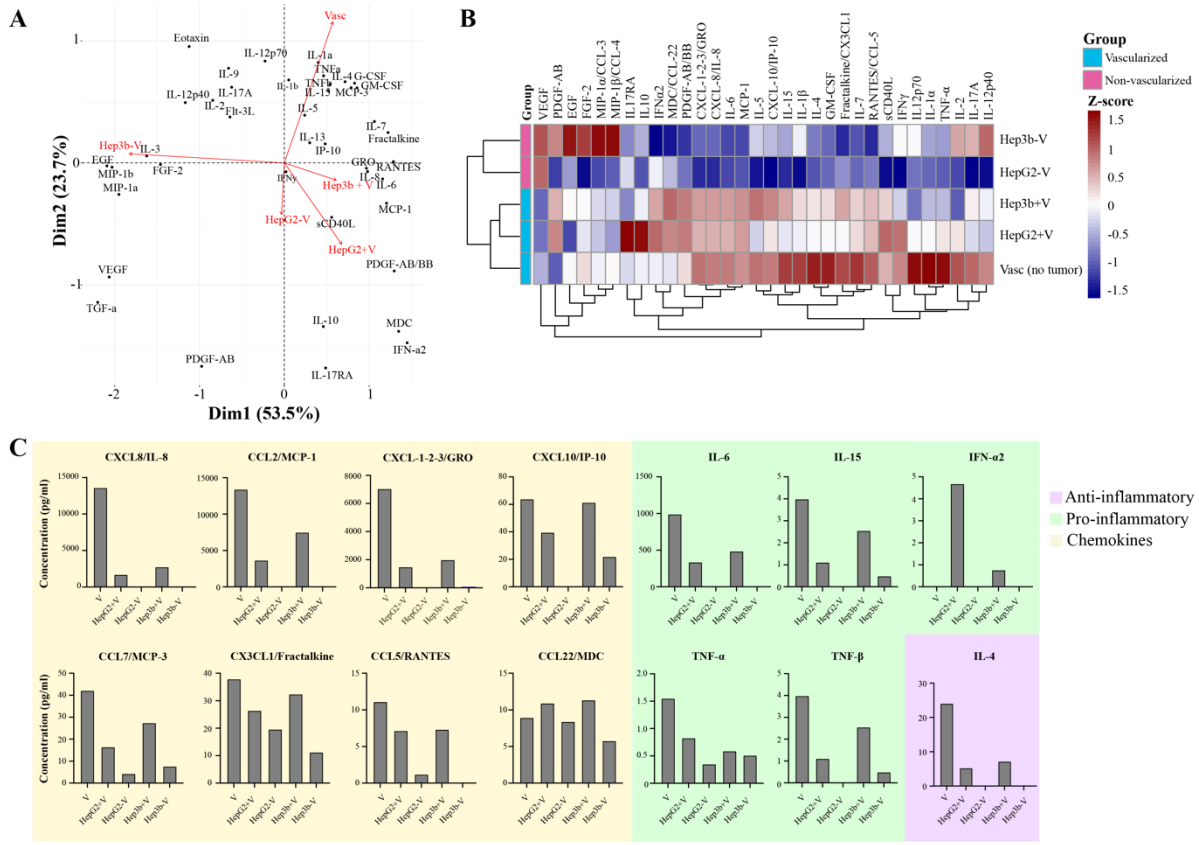

Fig. 7: Luminex multiplex ELISA assay of conditioned media. (A) Principal component analysis (PCA) biplot of cytokines (black dots) measured in five samples (red vectors). Cytokine values were normalized to the z-scores. The X- and Y-axes are plotted as two principal components (Dim 1 and Dim 2). PCA was plotted using the R package factoextra, which is freely available under a GPL-2 license. (B) Heatmap of cytokines in the five sample variants. Unsupervised hierarchical clustering classifies samples into two distinct groups: vascularized and avascular. Heatmap was plotted using the R package pheatmap which was freely available under a GPL-2 license; (C) Concentration (pg/ml) of chemokines and immune mediators in conditioned media Pooled media from two devices in each group were used for analysis.

Spatial mapping of T-cell distribution and functional characteristics within Hep3b tumors through multiplex imaging

Spatial analysis of T-cell distribution within the tumor microenvironment can help better correlate their functions with specific locations. To validate our flow cytometry findings, tissue cryosections of vascularized and avascular Hep3b tumors treated with CD133+ CAR-T cells were subjected to cyclic immunofluorescence staining using MACSima multiplex imaging technology (MICS) (Fig. 8A). This involves repeated cycles of staining and bleaching, enabling the assessment of numerous antibody targets on a single tissue slice. Tumor cryosections were stained with a large panel of biomarkers, and we specifically surveyed staining for nuclei, tumor cells, vascular networks, and T cell populations. DAPI was used to identify nuclei across the entire tissue region. CD326 (EpCAM) stained the tumor region, and collagen IV identified the vasculature in both ECM and intratumoral regions. CD8 marked the cytotoxic CAR-T cell subsets, whereas CD4, used to identify helper T cell subsets, did not stain within the cyclic imaging timeframe (10 min).

Three replicates for each condition examining vascularized and avascular Hep3b tumors were selected for MICS, encompassing six regions of interest (ROIs) in total. ROIs were selected to

cover the surrounding TME along with the entire tumor, comprising the tumor margins and core (Fig. 8B). Images of the whole tumor region stained with various antibodies are shown in Fig. S9, S10. Consistent with our earlier findings, we observed an increased infiltration of CD8+ T-cells within avascular Hep3b tumors (Fig. 8D). The activated T-cell population was defined by gating for CD8+ cytotoxic T-cells expressing the marker CD44[36]. Both vascularized and avascular T-cells showed similar levels of activation (Fig. 8E). Exhausted T-cells were defined by gating CD8+ cytotoxic T-cells expressing the marker CD162 (PSGL-1)[37]. T-cells that transmigrated through the endothelium and infiltrated the tumors showed significantly lower levels of the immune checkpoint molecule, CD162, compared to avascular tumors (Fig. 8F). This further confirms our results from flow cytometry, where we observed a reduction in exhaustion markers within T-cell populations that have extravasated the endothelial barrier.

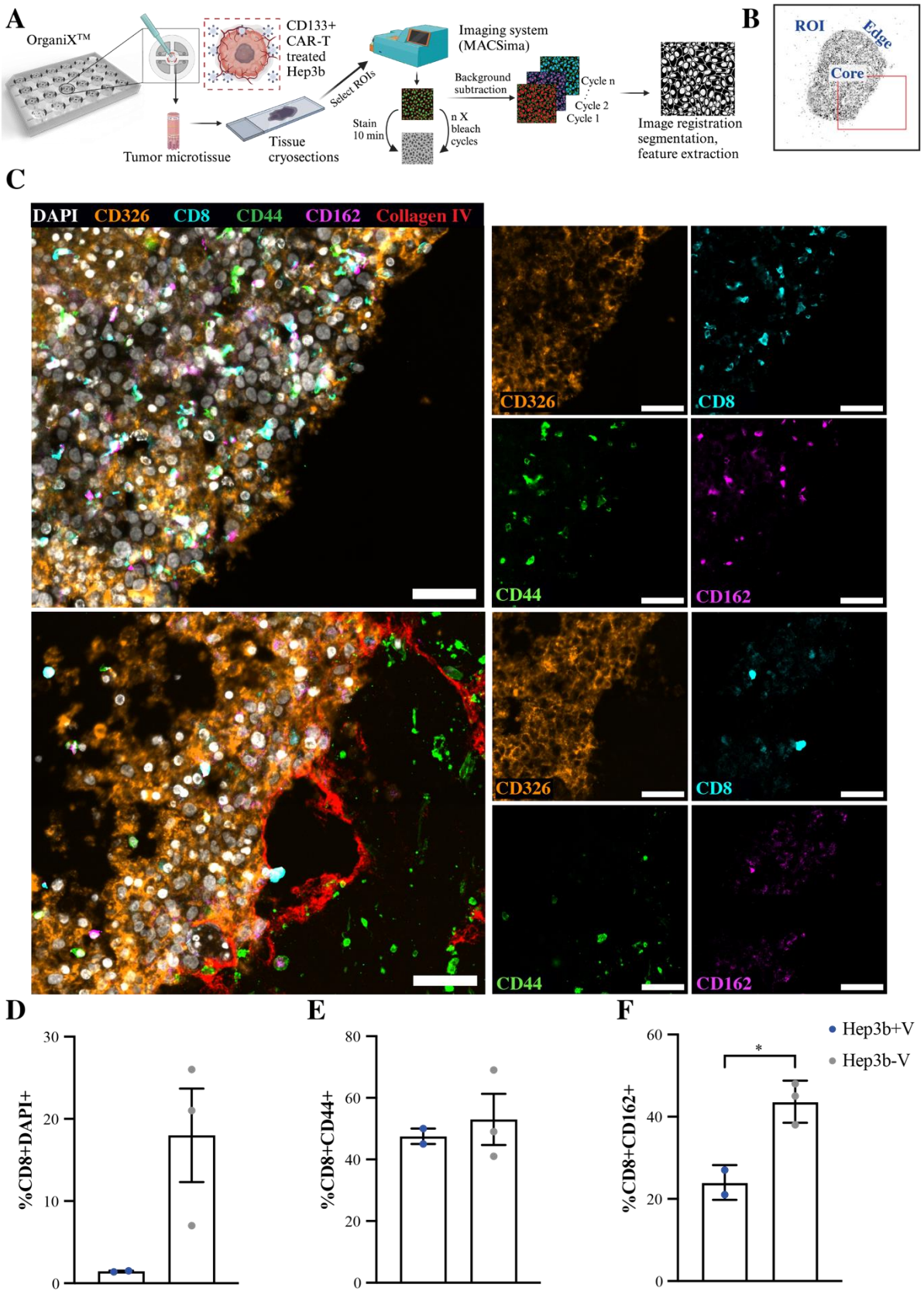

Figure 8: High-content multiplex imaging of vascularized and non-vascularized Hep3b tumor spheroids using MICS technology. (A) Workflow of multiplexed immunofluorescence (IF) imaging using MICS technology. Cryosections of vascularized and non-vascularized Hep3b tumors treated with CD133+ CAR-T cells were placed on slides, fixed, and permeabilized before ROI selection using DAPI staining. The sections were

iteratively stained and photobleached for a large number of antibody targets within the same tissue slice. Post staining, image registration and segmentation were performed, and relevant features were extracted for further analysis; (B) Inverted mask image (top) showing the entire tumor region and zoomed insets of the selected ROI stained for various markers are shown in the panels below; (C) Zoomed insets of the selected ROI stained for nuclei (DAPI, white/gray), tumor region (CD326, orange), vasculature (Collagen IV, red), cytotoxic T-cells (CD8, cyan), T-cell memory/activation (CD44, green) and T-cell immune checkpoint (CD162 or PSGL-1, magenta). Spatial mapping of each annotated biomarker is shown below the representative ROI images. Scale bar = 50 µm; (D) Quantification of %CD8+ cells relative to the number of DAPI+ cells present within the tumor region; (E) Quantification of %CD44+ cells relative to the %CD8+ cells present within the tumor region; (F) Quantification of %CD162+ cells relative to the %CD8+ cells present within the tumor region. Statistical significance was determined using Student's t-test with a confidence level of $\alpha = 0.05$. * = $p \leq 0.05$, ** = $p \leq 0.01$, *** = $p \leq 0.001$, **** = $p \leq 0.0001$.

Characterizing diversity within HepG2 tumors and their surrounding immune context using spatial transcriptomics

Microtissue sections from the device containing vascularized and avascular HepG2 tumor spheroids after co-culture with TCR+T cells were extracted for spatial transcriptomic analysis. This technology helps preserve native tissue architecture, thereby allowing the assessment of cellular states in a precise spatial context. Tissue sections were prepared for the GeoMx NanoString Cancer Transcriptome Atlas (CTA) panel and fluorescently labeled tumor morphology markers (Fig. 9A). CTA panel assays for 1800 genes were involved in modulating the tumor-immune microenvironment and tumor response to therapy. Morphological markers were used to select regions of interest (ROIs) inside the tumor and surrounding microenvironment for RNA quantification (Fig. 9B). ROIs were selected within tumors from vascularized and avascular models ("Tumor with vasculature" and "Tumor only," respectively) or in the vascular region from the vascularized model ("ECM"). The three regions had distinct gene expression profiles that were segregated using hierarchical clustering and principal component analysis (Fig. 9C, D). Notably, the genes in the "Tumor with vasculature" ROIs tend to cluster between the genes in the "Tumor only" ROIs and "ECM" ROIs.

We compared the overall gene expression profile to characterize the differences between the "Tumor with vasculature" ROIs and the "ECM" ROIs (Fig. 9E). The fold changes of various genes (log2 fold change, $p<0.05$) expressed are listed in Nanostring source data file (Supplementary Table 1). The top modulated genes in the "ECM" ROIs include collagens (COL1A2, COL6A3, COL5A1)[38-40], genes associated with the HCC TME (ANXA1, APP, CD44, CD81) [41-44], and vasculature formation (THBS1) [45-47]. "Tumor with vasculature" ROIs consist of genes associated with tumor-specific metabolism (ALDOA) [48], HCC-associated genes (SERPINA1, SPP1, APOA1, APOA2, AMBP, A2M) [49], and tumor hypoxia (VEGFA, ALDOA, ERO1A) [50-53].

Next, we compared the gene expression profiles between "Tumor with vasculature" ROIs and "Tumor without vasculature" ROIs (Fig 9F). The fold changes of various genes (log2 fold change, $p<0.05$) expressed are listed in Nanostring source data file (Supplementary Table 2). "Tumors with vasculature" exhibited higher expression of genes associated with HCC stroma such as collagens (COL1A1, COL1A2, COL6A3, COL5A1, COL3A1), angiogenesis (VEGFA), as well as those associated with the HCC TME and tumorigenicity (LOXL2, ITGA5, S100A9, CD81, APP) [54]. Of note are genes associated with inflammation (NFKBIA, TNFSF25, and IL4R) [55, 56] and cytotoxicity (CCL20, PRF1, and DEFB1)[57, 58]. These results indicate that the vascularized tumor model, which is a major obstacle for infiltrating TCR+T cells, could be immunogenic and enhance antitumor activity. Avascular tumor spheroids showed higher expression of liver-associated genes (RBP4, APOA1/2, and APOB)

and genes associated with cancer and HCC (KRAS, H3C10, H3C2, and ID1)[49, 59, 60] than vascularized spheroids. Fold changes of genes (log2 fold change, $p<0.05$) related to T-cell responses and inflammation are shown in Fig. S11 and the data are listed in Nanostring source data file (Supplementary Table 3).

Analysis of spatial gene expression in the "Tumor with vasculature" ROIs following TCR+ T cell therapy revealed enrichment for genes within the gene ontology (GO) terms "ECM organization," "immunoregulatory interactions," "interleukin, interferon and cytokine signaling" (Fig. 9G). Notably, TNFRSF25 (DR3) expression in vascularized tumors may indicate cytokine production via TL1A/DR3 signaling. Whereas, in the "Tumor only" ROIs the enriched GO keywords include "metabolism" and "cellular response to stress and hypoxia," which is in line with the fact that the core of avascular tumors is less viable and more susceptible to cell death.

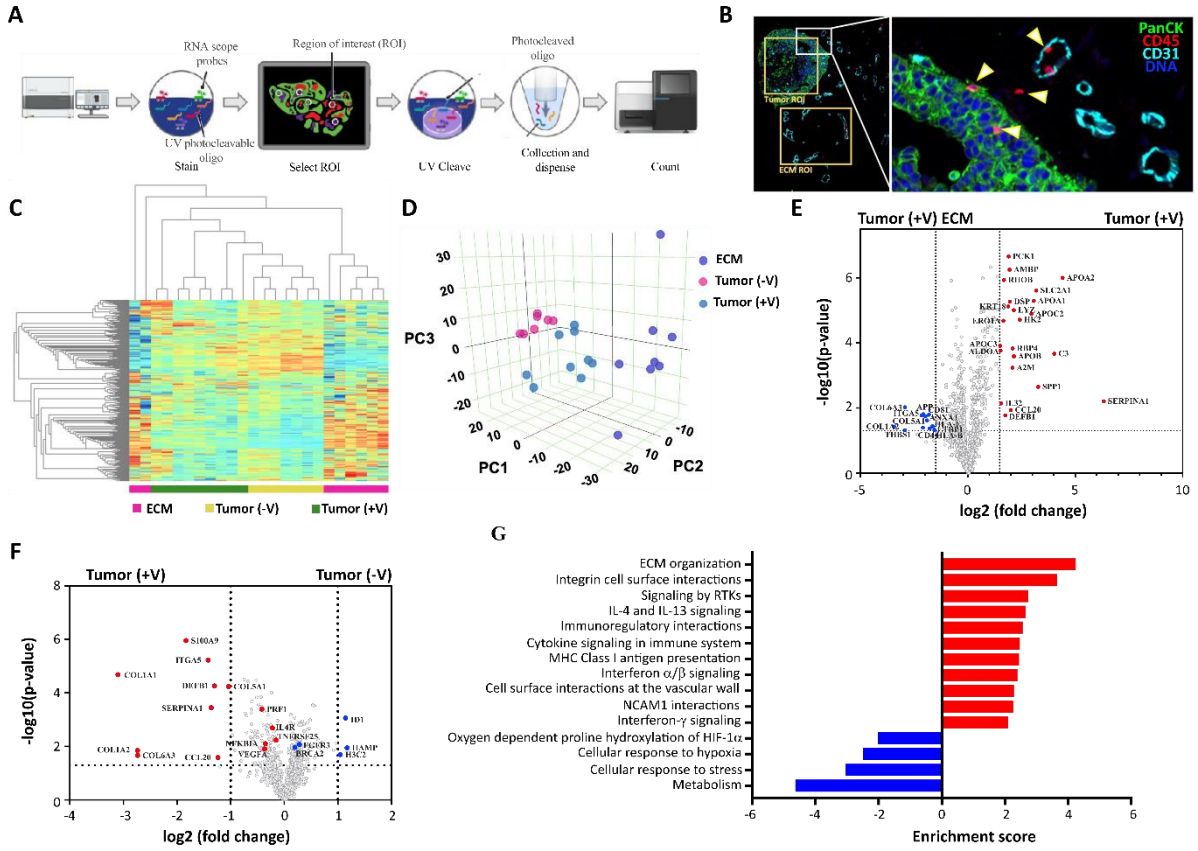

Fig. 9: Nanostring DSP assay. (A) Workflow of NanoString DSP analysis; (B) Image of fluorescently labelled tissue sections indicating tumor and ECM regions of interest (ROIs). Tumor cells are labelled with PanCK (green), T-cells are labelled with CD45 (red), endothelial cells are labelled with CD31 (cyan) and nuclei with DAPI (blue); (C) Gene expression profiles for tumor regions, tumor regions within vasculature and ECM regions presented as a hierarchical clustering map; (D) Principal component analysis for gene expression profiles for tumor, vascularized tumor, and ECM regions; (E) Volcano plot of genes differentially expressed in vascularized tumors (labelled as "Tumor with vasculature") and their surrounding ECM (labelled as "ECM"); (F) Volcano plot of genes differentially expressed in vascularised tumors (labelled as "Tumor with vasculature") and avascular tumours (labelled as "Tumor only"); (G) Fold enrichment of pathways that were significantly upregulated or downregulated between tumor regions in models with (red bars) and without (blue bars) vasculature ($p<0.05$).

Discussion

In vitro vascularized tumor models are emerging as vital microphysiological systems that enhance therapeutic discovery pipelines, particularly through our innovative OrganiX™ platform[23]. Building upon established 3D microfluidic models[24-26], OrganiX™ distinguishes itself through its 24-well design with removable inserts, enabling both automated high-throughput analyses and diverse downstream assays. The platform's large scale and open design accommodate tumors up to 2 mm in diameter, exceeding the capacity of previous microfluidic models, which are typically limited to a few hundred microns in height [25, 61-63]. This scale enables better recapitulation of tumor biology, including hypoxic/necrotic cores and dense vascular networks to regulate nutrient and oxygen gradients. Its user-friendly design leverages gravity-driven media flow, thereby eliminating the need for complex pumping systems[64, 65]. OrganiX™ offers remarkable versatility for downstream analyses, including histology, spatial biology, flow cytometry, and multi-omics for immunophenotyping and molecular profiling. The platform can be adapted to diverse research needs and facilitates high-throughput analyses with various cell types, making it a powerful tool for accelerating the development of targeted therapies.

In this study, we utilized two liver tumor cancer cell lines, HepG2 and Hep3b (the two most frequently used liver cancer cell lines in cancer research), to understand the role of TME in modulating treatment responses. The dimensions of the spheroids generated using the hanging drop technique were carefully optimized by varying the number of cells in the initial cell suspension to ensure diameters > 500 µm to recapitulate a hypoxic core based on previous reports [66, 67]. TME complexity was enhanced by co-culturing these spheroids with stromal cells, endothelial cells and fibroblasts, within a collagen-fibrin matrix. These stromal cells self-assembled to form perfusable vascular networks that extensively covered the tumor periphery, with vessels encompassing ~70% of the surrounding area. The measured vascular permeability (~ 1.8 x 10^{-7} cm/s) in our devices closely align with *in vivo* values, making it particularly suitable for drug delivery studies [68, 69]. Although we are still far from mimicking the complexities of human tumor tissue in its entirety, the model recapitulated tissue properties that are some key determinants of therapeutic efficacy: (1) a hypoxic tumor core, (2) an extracellular matrix, and (3) perfusable vascular networks. The tumor microtissues can be cultured within this platform for up to 2 weeks to study tumor-vascular interactions. Extending this time period led to the collapse of endothelial barriers, likely due to the inherent limitations of using primary HUVECs. Future iterations will explore alternative endothelial cell sources, such as immortalized cells or induced pluripotent stem-cell (iPSC) derived endothelial cells. This advancement would enable longer-term studies and expand the scope of our investigations.

Distinct differences in vascular network architecture were observed between the tumor types, likely reflecting their underlying genetic heterogeneity[70]. The presence of a vascular network enhanced tumor cell proliferation, which aligns with the canonical understanding that solid tumors secrete factors to promote vascularization and improve their overall survival[71, 72]. Growth factor signaling pathways such as VEGF and Angiopoietin/tie promote neoangiogenesis [73, 74]. The rapid expansion and vascularization of tumors lead to metabolic reprogramming, changing the cells' metabolic and phenotypic states to accommodate growth[75]. Interestingly, the presence of vasculature significantly reduces hypoxia within the both the tumor variants, likely due to the improved delivery of oxygen and nutrients to the tumor core. This reduction in hypoxia is crucial because it influences a multitude of processes critical to tumor progression and therapeutic response including cellular metabolism, ECM

remodeling and therapy resistance[76, 77]. Vascular remodeling differences may also arise from variations in angiogenic factor levels (e.g., EGF, FGF-2, PDGF) within the conditioned media, in addition to genetic and molecular heterogeneity[78]. These proangiogenic factors work in concert to enhance tumor-vasculature anastomoses, support tumor growth, and potentially facilitate tumor metastasis[78].

In our model, sorafenib effectively normalized tumor vasculature, inducing endothelial cell apoptosis within 48 hours in both HepG2 and Hep3b tumor microenvironments. This anti-angiogenic effect is consistent with the drug's known inhibition of VEGF signaling, among other targets[79]. We also observed that the two tumor subtypes displayed distinct responses to the drug. HepG2 tumors, despite minimal tumor-vasculature interaction, exhibited substantial death in the tumor core. In contrast, Hep3b tumors remained largely intact, with sorafenib primarily affecting cells at the periphery. This reflects the clinical heterogeneity of treatment outcomes influenced by factors like disease etiology[80]. Notably, the treatment resulted in incomplete tumor eradication in both the tumor types. While extended sorafenib treatment warrants further investigation, our observations align with findings from HCC patients and mouse tumor models, where complete tumor eradication is rare despite treatment with elevated doses for prolonged time periods [81-84]. This suggests that tumor-ECM interactions may contribute to resistance mechanisms, counteracting initial tumor regression. Future studies with this model could explore potential resistance mechanisms, such as dynamic alterations in hypoxia pathways, genetic adaptations within tumor cells [85], and upregulation of inflammatory mediators like IL-6 and CCL-22[86-88]. Incorporating periodic drug replenishment or patient-derived xenografts (PDXs) could further enhance the model's clinical relevance and provide insights into overcoming treatment resistance. Our model offers a simplified and controlled platform to unravel the specific contribution of tumor vasculature to treatment response, which would be exceedingly difficult to isolate from *in vivo* environments.

We further utilized our model to evaluate the efficacy of CD133+ CAR-T cell therapy, an emerging treatment modality for HCC. Upon treatment of tumors with CD133+ CAR-Ts, we found that the tumor endothelium forms a physical barrier around the tumor and reduces the number of infiltrating T-cells targeted to Hep3b spheroids. However, despite this limited infiltration, CAR-T cells that successfully reached the tumor region retained their cytotoxic function and effectively induced tumor cell death. This paradoxical observation highlights the dual role of the tumor vasculature in CAR-T therapy. Similar observations were made in mouse xenograft models where CD133+ CAR-T therapy significantly reduced tumor growth[32], with a potential to be enhanced using PD-1 scFv checkpoint inhibitors[89]. Multiple infusions could improve the accumulation of CAR-T within the tumor region [11, 90], suggesting a potential avenue to correlate our results with patient findings. Despite the promising preclinical results, the clinical translation of CAR-T cell therapy for HCC faces hurdles. A major contributor to the high failure rate of promising treatments in clinical trials is the insufficient knowledge of key microenvironmental factors that influence therapeutic response. To address these limitations and improve clinical outcomes, there is a critical need for more advanced preclinical models, such as ours, that utilize human-derived cells and functional vasculature to better recapitulate the TME. While other models, such as the inverse opal scaffold approach[91], offer valuable insights into specific aspects of the TME, our platform provides a unique combination of features, including perfusable vasculature with *in vivo*-like permeability, a hypoxic tumor core, and compatibility with diverse analytical techniques, making it particularly well-suited for evaluating therapeutic efficacy.

Although CAR-T cell expansion in patients' peripheral blood suggests activation[89], their activity at the tumor site remained unclear. Our model provides a potential explanation: CAR-T cells that have successfully infiltrated the TME exhibited significantly reduced exhaustion markers (PD-1 and LAG-3), indicating enhanced functionality within the region. This reduction in exhaustion markers could be attributed to the presence of IL-7, IL-15, CXCL10, and CCL5 within the tumor microenvironment, known to enhance T-cell persistence and prevent exhaustion[92-94]. Overall, our platform bridges these gaps by offering a controlled environment to precisely dissect the mechanisms by which the endothelium influences tumor responses to therapy. Incorporating a longitudinal analysis of secretory factors within the conditioned media could allow identification of potential biomarkers that could predict likelihood of achieving complete response in tumors[95]. Combination therapy to normalize the vasculature prior to treatment with engineered T-cells can be further studied using this microphysiological system[96]. Co-culturing myeloid-derived suppressor cells, hepatic stellate cells, macrophages or neutrophils within this model can help further enhance the complexity of this system to create an immunosuppressive microenvironment[91, 97, 98].

Cyclic imaging showed reduced levels of the immune checkpoint molecule CD162 (PSGL-1) in vascularized Hep3b tumors. PSGL-1 is a cell adhesion molecule expressed on T-cells and is primarily known for its role in leukocyte trafficking. It mainly binds to selectins (P-selectin and E-selectin) on endothelial cells, facilitating the initial tethering and rolling of leukocytes along blood vessel walls[37]. Studies in disease models, such as melanoma and cervical carcinoma, have shown that PSGL-1 ligation with TCR upregulates PD-1 expression in T-cells, thereby driving them to an exhaustive state[99-101]. The mechanisms with which the endothelium can reduce PSGL-1 expression in T-cells are yet to be confirmed and require further validation studies. Our model highlights that PSGL-1 may serve as a promising new target for the treatment of liver tumors. Further validation includes assessing functional consequences of PSGL-1 reduction on T-cell activation and anti-tumor activity by employing blocking antibodies in *in vitro* and *in vivo* environments.

The engineered TCR+ T cell assay also confirmed the important role of the vasculature during cell therapy. Similar to the results obtained with CAR-T cell treatment on Hep3b tumors, the infiltration levels of TCR+T cells were significantly lower in vascularized HepG2 spheroids than in their avascular counterparts. TCR+T cell induced tumor death for both vascularized and avascular HepG2 was insignificant. TCR+T cells were designed to stably and transiently express exogenous TCR and, therefore, may only offer a limited antitumor effect that eventually diminishes with the onset of exhaustion[13]. Further assessment by periodically refreshing the TCR+T cell population within the coculture model using multiple doses at regular intervals may help to determine whether antitumor activity can be improved.

Spatial transcriptomic analysis from distinct ROIs segregated the samples into different clusters, providing valuable insight into how the molecular profiles of tumors change due to intrinsic tumor cell properties and differences between tumors and the surrounding stromal composition. The increased expression of TNFRSF25 (DR3) in vascularized tumors provides further evidence supporting our observations regarding the proinflammatory nature of the TME. TNFRSF25 is a costimulatory receptor expressed on T-cells that, when activated by its ligand TL1A, can enhance T-cell proliferation, cytokine production, and effector functions[102]. The presence of TNFRSF25 in vascularized tumors may indicate an environment conducive to T-cell infiltration and activation. Evidence in mouse myeloma model has shown that treatment with TNFRSF25 agonists demonstrate high anti-tumor efficacy in tumors infiltrated with T-cells. This suggests that the increased expression of

TNFRSF25 could be leveraged to enhance the effectiveness of immunotherapies targeting these tumors[103].

In conclusion, we developed an *in vitro* vascularized solid tumor model that can recreate key features of the TME. As this system was developed with human cell lines, it cannot fully replicate the intricacies of *in vivo* tumors. However, it serves as a valuable complementary platform to refine therapeutic strategies before animal testing. This approach has the potential to reduce animal usage and expedite the translation of promising therapies to the clinic. A key advantage of this system lies in its ability to precisely manipulate the tumor microenvironment, allowing for systematic investigation of tumor-stroma interactions and treatment response by controlling factors such as oxygen tension, nutrient gradients, and cellular composition. By providing a controlled microenvironment, this approach offers a proof-of-concept for utilizing vascularized tumor models to gain insights into the role of the TME in modulating drug and cell therapy responses. While our study focuses on human cell lines, the model's versatility allows for the incorporation of patient-derived xenografts in future studies. This will enable a more personalized approach to investigating tumor behavior and treatment responses, capturing the inherent heterogeneity of HCC and potentially guiding the development of tailored therapeutic strategies.

Materials

Key resources table

RESOURCE/REAGENT	SOURCE	CATALOG NUMBER/IDENTIFIER
Experimental Model: Cell lines		
HepG2-GFP	Provided by Antonio Bertoletti lab	
Hep3b-GFP	Provided by Philip Kaldis lab	
nHLF	Lonza	CC-2512
HUVEC-GFP	Vector Biomed	CAP0001GFP
Antibodies		
CD25 BV605	Life technologies	406-0459-42
HLA-DR BUV737	Life technologies	367-9956-42
LAG-3 BUV395	Life technologies	363-2239-42
PD-1 BV421	Zuellig Pharma	562516
TIM-3 BV711	Zuellig Pharma	565566
IFNg PE-Cy7	Zuellig Pharma	560741
TNFa AF700	Zuellig Pharma	557996
GznB PE	Zuellig Pharma	561142
CD3 Monoclonal antibody	eBioscience	16-0037-81
Anti-cleaved caspase-3	Cell Signaling	9661
anti-Ki67	Cell Signaling	9449
anti-Hif-1α	Cell Signaling	36169
Alexa Fluor™ 405 Goat Anti-Mouse IgG	Invitrogen	A-31553
Alexa Fluor™ 647 Goat Anti-Rabbit IgG	Invitrogen	A32733
Pan cytokeratin PE (PanCK-PE)	Invitrogen	MA5-28574

mouse anti-human CD31 Alexa Fluor™ 647	BioLegend	303112
rat anti-human CD45	Invitrogen	MA5-17687
Goat anti-rat Alexa Fluor™ Plus 405	Invitrogen	A48261
Chemicals, growth factors		
RPMI 1640, no glutamine	Gibco	21870076
Fetal bovine serum, heat inactivated	Gibco	16140071
N-2-hydroxyethylpiperazine-N-2-ethane sulfonic acid (HEPES)	Gibco	15630080
Penicillin/Streptomycin	Gibco	15140122
Minimum essential medium (MEM) amino acid solution	Gibco	11130051
Sodium Pyruvate	Gibco	11360070
0.25% Trypsin-EDTA	Gibco	25200056
Collagenase, Type IV	Gibco	17104019
Nattokinase	Japan Bio Science Laboratory	
DNase I recombinant, RNase-free	Roche	04716728001
MEM non-essential amino acid solution	Gibco	11140050
GlutaMAX	Gibco	35050061
Plasmocin	Invitrogen	ant-mpt
Puromycin	Singlab Technologies	631305
Dulbecco's modified eagle's medium (DMEM, high glucose)	Gibco	11960044
EGM-2 medium	Lonza	CC3162
Interleukin-2 (IL-2)	Miltenyi Biotech	130097746
AIM-V	Gibco	12055091
human AB serum	Sigma-Aldrich	H6914
scFv-CD28-CD3ζ-T2A-RFP-CD133 plasmid	Creative Biolabs, USA	N/A
Thrombin	Sigma Aldrich	T7513
Fibrinogen	Sigma Aldrich	F8630
Collagen I, Rat Tail	Corning	354236
Vascular endothelial growth factor (VEGF)	Singlab technologies	293-VE-050
Dextran Texas Red™ 70 kDa (25 mg/ml)	Invitrogen	D1864
Sorafenib	Cayman Chemical	10009644
Dimethyl sulfoxide (DMSO)	Sigma-Aldrich	D8418
DRAQ7	Abcam	ab109202
Formaldehyde (FA)	Life technologies	28908

Triton X-100		
Bovine Serum Albumin (BSA)	MP Biomedicals	MPB#0216006980
Phosphate-Buffered Saline (PBS)	Gibco	20012027
Goat serum	Gibco	50062Z
Rapiclear	SunJin Labs	RC149002
Live/Dead Fixable Near-IR Dead Cell Stain Kit	Invitrogen	L10119
BD Cytofix/Cytoperm ()	BD Biosciences, USA	554722
isopentane (2-methylbutane)	Sigma Aldrich	277258
Software and algorithms		
ImageJ/Fiji	https://imagej.net/software/fiji/	N/A
RStudio 4.3.0	https://cran.rstudio.com/	N/A
Biorender	https://www.biorender.com/	N/A
FlowJo	https://www.flowjo.com/	N/A
GraphPad Prism	https://www.graphpad.com/	N/A
MACS iQ View	https://www.miltenyibiotec.com/SG-en/products/macs-iq-view-spatial-biology-software.html	N/A
GeoMx® DSP	https://nanostring.com/products/geomx-digital-spatial-profiler/geomx-dsp-overview/	N/A

747

RESOURCE/REAGENT	**SOURCE**	**CATALOG NUMBER/IDENTIFIER**
Experimental Model: Cell lines		
HepG2-GFP	Provided by Antonio Bertoletti lab	
Hep3b-GFP	Provided by Philip Kaldis lab	
nHLF	Lonza	CC-2512
HUVEC-GFP	Vector Biomed	CAP0001GFP
Antibodies		
CD25 BV605	Life technologies	406-0459-42
HLA-DR BUV737	Life technologies	367-9956-42
LAG-3 BUV395	Life technologies	363-2239-42
PD-1 BV421	Zuellig Pharma	562516
TIM-3 BV711	Zuellig Pharma	565566
IFNg PE-Cy7	Zuellig Pharma	560741
TNFa AF700	Zuellig Pharma	557996
GznB PE	Zuellig Pharma	561142
CD3 Monoclonal antibody	eBioscience	16-0037-81
Anti-cleaved caspase-3	Cell Signaling	9661
anti-Ki67	Cell Signaling	9449
anti-Hif-1α	Cell Signaling	36169
Alexa Fluor™ 405 Goat Anti-Mouse IgG	Invitrogen	A-31553

Alexa Fluor™ 647 Goat Anti-Rabbit IgG	Invitrogen	A32733
Pan cytokeratin PE (PanCK-PE)	Invitrogen	MA5-28574
mouse anti-human CD31 Alexa Fluor™ 647	BioLegend	303112
rat anti-human CD45	Invitrogen	MA5-17687
Goat anti-rat Alexa Fluor™ Plus 405	Invitrogen	A48261
Chemicals, growth factors		
RPMI 1640, no glutamine	Gibco	21870076
Fetal bovine serum, heat inactivated	Gibco	16140071
N-2-hydroxyethylpiperazine-N-2-ethane sulfonic acid (HEPES)	Gibco	15630080
Penicillin/Streptomycin	Gibco	15140122
Minimum essential medium (MEM) amino acid solution	Gibco	11130051
Sodium Pyruvate	Gibco	11360070
0.25% Trypsin-EDTA	Gibco	25200056
Collagenase, Type IV	Gibco	17104019
Nattokinase	Japan Bio Science Laboratory	
DNase I recombinant, RNase-free	Roche	04716728001
MEM non-essential amino acid solution	Gibco	11140050
GlutaMAX	Gibco	35050061
Plasmocin	Invitrogen	ant-mpt
Puromycin	Singlab Technologies	631305
Dulbecco's modified eagle's medium (DMEM, high glucose)	Gibco	11960044
EGM-2 medium	Lonza	CC3162
Interleukin-2 (IL-2)	Miltenyi Biotech	130097746
AIM-V	Gibco	12055091
human AB serum	Sigma-Aldrich	H6914
scFv-CD28-CD3ζ-T2A-RFP-CD133 plasmid	Creative Biolabs, USA	N/A
Thrombin	Sigma Aldrich	T7513
Fibrinogen	Sigma Aldrich	F8630
Collagen I, Rat Tail	Corning	354236
Vascular endothelial growth factor (VEGF)	Singlab technologies	293-VE-050
Dextran Texas Red™ 70 kDa (25 mg/ml)	Invitrogen	D1864
Sorafenib	Cayman Chemical	10009644

Dimethyl sulfoxide (DMSO)	Sigma-Aldrich	D8418
DRAQ7	Abcam	ab109202
Formaldehyde (FA)	Life technologies	28908
Triton X-100		
Bovine Serum Albumin (BSA)	MP Biomedicals	MPB#0216006980
Phosphate-Buffered Saline (PBS)	Gibco	20012027
Goat serum	Gibco	50062Z
Rapiclear	SunJin Labs	RC149002
Live/Dead Fixable Near-IR Dead Cell Stain Kit	Invitrogen	L10119
BD Cytofix/Cytoperm ()	BD Biosciences, USA	554722
isopentane (2-methylbutane)	Sigma Aldrich	277258
Software and algorithms		
ImageJ/Fiji	https://imagej.net/software/fiji/	N/A
RStudio 4.3.0	https://cran.rstudio.com/	N/A
Biorender	https://www.biorender.com/	N/A

Methods

Cell culture

Green fluorescent protein (GFP) tagged HepG2-PreS1 (HepG2) cells were cultured in R10 media (RPMI 1640 no glutamine (Gibco)) supplemented with 10% heat-inactivated fetal bovine serum (FBS), 20 mM N-2-hydroxyethylpiperazine-N-2-ethane sulfonic acid (HEPES), 100 U/mL penicillin, 100 µg/mL streptomycin, 1x minimum essential medium (MEM) amino acid solution, 1mM sodium pyruvate, 1x MEM non-essential amino acid solution, 1x GlutaMAX, and 5 µg/mL plasmocin (InvivoGen). Puromycin (5 µg/mL, Takara) was added for selection during cell culture. GFP tagged Hep3b (Hep3b) cells were grown in complete Dulbecco's modified Eagle's medium (DMEM) containing high glucose DMEM (Gibco) supplemented with 10% heat-inactivated FBS and 1% penicillin/streptomycin. Normal human lung fibroblasts (NHLF) (Lonza, Basel, Switzerland) were cultured in complete DMEM. GFP-tagged human umbilical vein endothelial cells (HUVEC) (Lonza) were cultured in EGM-2 medium supplemented with 5% heat-inactivated FBS and 1% penicillin/streptomycin. Primary cells were used before passage 7.

T-cell isolation

To obtain T-cells, peripheral blood mononuclear cells (PBMCs) were isolated from healthy donors by Ficoll (GE Healthcare, USA) density gradient centrifugation according to the manufacturer's instructions. The PBMCs were stimulated with 600 IU/ml interleukin-2 (IL-2) (Miltenyi Biotec) and 50 ng/ml anti-CD3 (eBioscience) in AIM-V (Gibco) supplemented with 2% human AB serum (Sigma-Aldrich) for 9 days to allow T-cell expansion at 37°C and 5% CO_2. The expanded T-cells were collected by centrifugation and stored in liquid nitrogen until further use.

Tumor spheroid formation

Hep3b and HepG2 cells were cultured until confluence, trypsinized, and resuspended at a concentration of 7.2×10^5 and 6.5×10^5 cells/ml, respectively, in complete DMEM and R10

media. The hanging drop method was applied to form tumor spheroids: cells were seeded as 30-µl drops in a homemade polydimethylsiloxane (PDMS) hanging drop membrane on the inverted lid of a 96-well plate and then placed at 37 °C in a humidified incubator under 5% CO_2 atmosphere for 5 days.

HBV-S183 antigen specific T-cells generation

HBV envelope S183–191 TCR mRNA was produced using *in vitro* transcription as previously described. IL-2 was increased to 1000 IU/ml atleast 6 hrs before electroporation. T-cells were then electroporated with AgilePulse MAX (BTX). 1×10^7 T-cells were suspended in 200 µl of BTXpress cytoporation low conductivity medium T (BTX). 20 µg of HBV envelope S183–191 TCR mRNA was added per 1×10^7 of T-cells. After electroporation, the cells were allowed to recover at 37°C and 5% CO_2 overnight in AIM-V supplemented with 10% human AB serum and 100 IU/ml human recombinant IL-2 (IL-2). T-cells expressing the introduced TCR were quantified by flow cytometry using a TCR Vβ 3 FITC antibody (Beckman Coulter).

CD133-specific CAR-T cell generation

scFv-CD28-CD3ζ-T2A-RFP-CD133 plasmid (Creative Biolabs, USA) was used to generate CD133 CAR T-cells from PBMCs. Briefly, PBMCs were stimulated with 600 IU/mL IL-2 and 50 ng/mL anti-CD3 in AIM-V supplemented with 2% human AB serum for 4 days. CD133 CAR-T lentivirus particles were added to the T-cells at a multiplicity of infection (MOI) of 5 and cultured overnight in the presence of polybrene (8 µg/ml) and Dynabeads human T-activator CD3/CD28, according to the manufacturer's protocol. T-cells were then incubated for 4 days, and cells expressing RFP (CD133+ CAR-T) were isolated by sorting using a BD FACS Aria II (BD BioSciences). T-cells were expanded using AIM-V supplemented with 2% human AB serum for 9 days.

3D vascularized tumor spheroid formation

Interactions between immune cells and the complex 3D vascularized tumor microenvironment were studied using a commercially available easy-to-use 3D tissue culture platform (OrganiX, AIM Biotech). The platform comprises of 24 wells, each well containing a central gel region flanked by media channels on either side. The gel region contains the tumor spheroid cultured with or without vasculature in a collagen-fibrin gel network, and the media channels allow for the efficient delivery of nutrients and gas exchange.

The tumor spheroids were collected from the hanging drop membrane by centrifugation before being injected into the device. Thrombin stock was made at 100 U/ml and stored at - 80°C. Aliquots of collagen stock (3.57 mg/ml) and fibrinogen stock (6 mg/ml) were prepared and stored at 4°C and -80°C respectively. A resuspension medium was prepared using thrombin (1 U/ml) and collagen (0.4 mg/ml) diluted from their stock solutions using cold EGM-2 media. Microvascular networks were formed around the tumor spheroids using a co-culture of HUVEC and NHLF. HUVEC and NHLF were trypsinized, counted, and mixed in a resuspension medium at final concentrations of 8×10^6 HUVEC/ml and 2×10^6 NHLF/ml. The culture medium surrounding the tumor spheroids from hanging drops was completely removed and replaced with 25 µL of resuspension media containing the HUVEC-NHLF mixture. An equal volume of fibrinogen solution (6 mg/ml) was mixed with the spheroid and a total volume of 50 µL was aspirated and pipetted into the central gel region of the well. For devices without vascular networks, spheroids were mixed with cell-free resuspension medium and deposited into the central gel channel, along with fibrinogen. The fibrinogen, thrombin, and collagen mixtures were allowed to polymerize for 20 min at room temperature. After polymerization, EGM-2 supplemented with 50 µg/ml VEGF was added to the media channels for the first 3

days and changed daily. 4 days after device seeding, media were removed, and the side channels of devices with vascular networks were layered with 35 µl of HUVEC at 1×10^6 cells/ml and tilted at 45º on each side in the incubator for 15 min to allow formation of a HUVEC monolayer on the collagen-fibrin gel surface. For devices without vascular networks, cell-free EGM-2 was dispensed into the side channels. Fresh EGM-2 medium was replenished in the reservoirs, and the devices were incubated at 37 °C in a humidified incubator under a 5% CO_2 atmosphere.

Vessel characterization

All images were acquired on ZEISS LSM 800 and ZEISS LSM 880 confocal microscopes using Zeiss software, ZEN (blue edition). Vessel formation was monitored and measured over 7 days. Pictures were taken on days 1, 4, and 7 post-seeding, and FIJI was used to generate summed z-projections to calculate vessel formation by measuring the percentage coverage over time. Spheroid sizes were also measured as the areas of the spheroids over 7 days and compared to the avascular spheroids. Vessel branch and diameter analyses were carried out using the BranchAnalysis2D/3D plugin in FIJI.

Vessel perfusion and permeability

For vascular permeability measurements, dextran Texas Red™ 70 kDa (25 mg/ml) (Invitrogen) was diluted 1:100 in EGM-2 and perfused through the vessels by replacing the medium from one side channel with the medium containing dextran. Immediately thereafter, time-lapse Z-stack confocal images were captured (5 min intervals, 5 µm z-depth) with a ZEISS LSM 800 confocal microscope to assess leakage through the vascular barrier. Permeability (P) was calculated as previously published[104] and measured as the flux of dextran across the wall of the vascular network:

$$P = \frac{V_m}{SA\,\Delta I}\frac{\Delta I_m}{t}$$

where V_m and SA indicate the ECM volume and surface area of the vasculature respectively in the imaged volume, $\Delta I = I_{(v,1)} - I_{(m,1)}$ is the difference in fluorescence intensity between the vasculature and the ECM at time t = 1 and $\Delta I_m = I_{(m,2)} - I_{(m,1)}$ indicates increase in fluorescence intensity within the ECM during time interval t.

Sorafenib treatment

Cytotoxic responses of Hep3b and HepG2 cells to Sorafenib (Cayman Chemical) were initially evaluated using xCELLigence real-time cell analysis at 37 °C, 5% CO_2 atmosphere. 50000 cells were seeded on gold electrodes embedded at the bottom of an E-plate VIEW 16 (Agilent Technologies) and left to adhere for 30 min in the BSC. Subsequently, the e-plate was placed into the xCELLigence RTCA DP analyzer. The cells were allowed to recover for 24 h. Before the addition of sorafenib, 100 µL of the medium was removed from all the wells. Sorafenib diluted in DMSO at various concentrations (0.1 µM, 1.25 µM, 2.5 µM, 5 µM, 10 µM, 20 µM, 50 µM, and 100 µM) were added to the respective wells. The control wells were prepared using an equivalent concentration of DMSO. The control and drug-treated cells were incubated for another 72 h and the impedance was recorded at 15 min intervals. IC_{50} values were evaluated using the RTCA-DP software (Roche Diagnostics GmbH) using sigmoidal dose-response curves.

To obtain the IC_{50} values of sorafenib against Hep3b and HepG2 spheroids, one spheroid was suspended into each well of a 96-well white microplate (Corning) in a medium containing

RealTime-Glo MT Cell Viability Assay (Promega), prepared according to the manufacturer's instructions. The plate was incubated at 37 °C, 5% CO_2 atmosphere for 60 minutes before baseline luminescence was recorded using a Tecan Spark plate reader (Tecan). The same medium was used to dilute sorafenib to a range of concentrations (0.1 µM, 1.25 µM, 2.5 µM, 5 µM, 10 µM, 20 µM, 40 µM, 60 µM, 80 µM, 100 µM). Sorafenib was then added and luminescence was recorded every 24 h. All readings were performed with the Spark Controller software using an integration time of 1000 ms. The raw luminescence value of each well was offset by the background reading from wells containing medium without any cells before normalizing the 100% viability value to the average luminescence values of the spheroids without any treatment. The respective datasets for Hep3b and HepG2 were then fitted with a non-linear curve to identify the IC_{50} value for each cell line.

Vascularized and avascular spheroids in microfluidic devices were treated with 20 µM Sorafenib and DRAQ7 (1:300) was diluted in EGM-2 medium 7 days post-seeding. Confocal images were taken daily with a ZEISS LSM 880 microscope to assess the viability of the spheroids over time, as indicated by the DRAQ7 signal.

Immune cell therapy

TCR+T cells were resuspended at a density of 1×10^6 cells/ml in AIM-V medium with 1:100 DRAQ7 (Abcam, ab109202) before adding them to the devices. Devices with vascularized and avascular HepG2 spheroids were used as targets for the TCR+T cells. TCR+T cells were added to the devices by replacing the media from one side channel with 100 µl of T-cell suspension. Confocal images were taken with ZEISS LSM 800 after 18 hr of incubation, and the DRAQ7 signal was measured to determine the killing efficiency.

CD133+ CAR-T cells were resuspended at a density of 1×10^6 cells/ml in AIM-V medium with 1:300 DRAQ7, before being added to the devices. Devices with vascularized and avascular Hep3b spheroids were used as CAR-T cell targets. After 7 days of vasculogenesis, the medium was removed from one side channel, and 1×10^5 CAR-T cells were seeded in each device. Confocal images were taken using ZEISS LSM 800 until day 6 of culture. DRAQ7 measurements were used to determine the killing efficiency of the CAR-T cells over time.

Immunofluorescence

The primary antibodies and their corresponding concentrations used for immunostaining are as follows: Anti-cleaved caspase-3 (Cell Signaling, 9661), anti-Ki67 (Cell Signaling, 9449), and anti-Hif-1α (Cell Signaling, 36169) used in this study at a dilution of 1:800, 1:400 and 1:400 respectively. Pan cytokeratin PE (PanCK-PE) (Invitrogen), mouse anti-human CD31 Alexa Fluor™ 647 (BioLegend), and rat anti-human CD45 (Invitrogen) were used at a concentration of 1:100.

The secondary antibodies and their corresponding concentrations utilized are as follows: Alexa Fluor™ 405 Goat Anti-Mouse IgG (Invitrogen) and Alexa Fluor™ 647 Goat Anti-Rabbit IgG (Invitrogen) were used at a concentration of 1:500. Goat anti-rat Alexa FluorTM Plus 405 (Invitrogen) was used at a concentration of 1:200.

Preparation of cryosections

All devices were fixed overnight in 4% (v/v) formaldehyde (FA) in 1X PBS at 4°C. To visualize cell nuclei, tissues were stained with DAPI (1:1000 in 1X PBS) for 24 h and then dehydrated using a 30% (w/v) sucrose (company name) solution for an additional 24 h. The devices were flash frozen in 2-methylbutane (company name). The bottom layer was peeled

off and the frozen microtissues were punched into cryomolds containing OCT solution. The microtissues were incubated in OCT overnight for 4°C followed by repeating the flash freezing process to generate cryoblocks.

Immunostaining cryosections

Tissue cryosections of 10 μm thickness was loaded onto glass slides and staining was performed using caspase-3, Ki67 and HIF1α antibodies. Sections were permeabilized using 1X PBS containing Triton X-100 (0.1% v/v) (PBS-T) for 20 min, followed by incubation with blocking buffer (PBS-T with 10% v/v goat serum) for 30 min. Sections were incubated with Ki67, caspase-3 or Hif-1α overnight at 4°C. This was followed by washing (3X, 5 min intervals) with PBS-T and incubation with secondary antibodies for 2 hrs. All sections were mounted with 50% (v/v) glycerol and images were acquired using Zeiss LSM 800, 20X magnification.

Whole tissue staining

For immunostaining whole devices with Pan-CK (tumor region), and CD31 (vasculature) and CD45 (T-cells), all devices were fixed overnight in 4% (v/v) formaldehyde (FA) in 1X PBS at 4°C. Permeabilization with 0.1% (v/v) Triton X-100 in 1X PBS (PBS-T) was performed overnight at 4°C, followed by blocking with a solution containing 3% (v/v) bovine serum albumin (BSA) (Sigma Aldrich) and 10% (v/v) goat serum (Gibco) in 0.1% (v/v) PBS-T at room temperature for 1 hr. Primary antibodies diluted in 0.5% BSA (v/v) in PBS-T were added to the devices and incubated at 4°C for 2 days on a rocker. The devices were washed with 1X PBS 3X every 30 min at room temperature. Secondary antibodies diluted in 0.1% (v/v) BSA in PBS-T were added to the devices and incubated overnight at 4°C on a rocker. The devices were washed 5X every 30 min at room temperature with 1X PBS and cleared overnight at 4°C (Rapiclear, SunJin Labs). Confocal images were acquired using a ZEISS LSM 880 with 10X and 20X objectives. Image analysis was performed using Fiji software.

Flow cytometry profiling of T-cell characteristics

Sample preparation

To profile cytokine, activation and exhaustion marker profiles of T-cells that have transmigrated the endothelial barrier into the tumor region, we used an idenTx 3 (AIM Biotech) platform. Hep3b embedded in a collagen-fibrin matrix was seeded in the gel channel region. To create a vascularized tumor mimicking system, HUVECs were seeded into both side channels and incubated until the formation of an endothelial monolayer. CD133+ CAR-Ts were seeded into one of the side channels and left undisturbed at 37 °C, 5% CO_2 for 48 h. T-cells were then flushed out from the side channels with media and collected for flow cytometry profiling. Then, the tumor microtissues in the central gel region were digested to extract the T-cells embedded in the collagen-fibrin matrix. The following digestion buffer mix was prepared for digestion: 0.25% Trypsin EDTA (Gibco) containing Collagenase IV (1:10 v/v from stock concentration of 100 mg/ml) (Gibco), Nattokinase (1:100 v/v from stock concentration of 5000 FU/ml) (Japan Bio Science Laboratory) and DNase I (1:200 v/v) (Sigma Aldrich). After flushing the T-cells from the side channels, each device was filled with 200 μL of digestion buffer mix distributed unevenly between the two side channels and the microtissues were incubated at 37 °C, 5% CO_2 for 10 min. The devices were agitated every 5 min by pipetting the media and gel inlets. The cells from the digested gel were flushed out of the devices using media and collected for flow cytometry profiling.

A quantity of atleast 10^5 T-cells was utilized for analysis. Live and dead cells were distinguished using Live/Dead Fixable Near-IR Dead Cell Stain Kit (L10119, Invitrogen) at a

concentration of 1:1000. The cells were subsequently washed using FACS buffer (1X phosphate buffered saline (PBS) (Gibco) containing 1% (w/v) bovine serum albumin (BSA) (MP Biomedicals) and 0.1% (w/v) sodium azide (Sigma Aldrich). This is followed by staining for cell surface markers, CD25, HLA-DR, CCR7, CD45RO, LAG-3, TIM-3, PD-1, at a concentration of 1:50 for 30 min. The cells were washed with FACS buffer to remove the unbound antibodies and fixed with 1% formaldehyde (Life Technologies). Acquisition was performed using BD FACSAria II (BD BioSciences).

To characterize intracellular cytokines, the devices were treated with brefeldin A (1:1000) for 5 hrs prior to performing digestion of tumor microtissues. Following digestion, cells were simultaneously fixed and permeabilized using BD Cytofix/Cytoperm (554722, BD Biosciences, USA). Intracellular cytokine staining was performed using GznB, TNFa and IFNg antibodies at a concentration of 1:50 for 30 min. The cells were washed with FACS buffer to remove the unbound antibodies and fixed with 1% formaldehyde. Acquisition was performed using BD FACSAria II (BD BioSciences).

Data analysis

All data acquired were analyzed using FlowJo software (version 10.10.0, Becton Dickinson & Company (BD)). Compensation was performed using single-stained controls, and doublet discrimination was applied to exclude cell aggregates. Lymphocytes were gated based on their forward scatter (FSC) and side scatter (SSC) characteristics, and then further analyzed for expression of CD3 to identify T-cell subsets. Boolean gating was used to identify CD3+ T cells expressing activation (CD25, HLA-DR) and exhaustion (PD-1, LAG-3 and TIM-3) markers. CD3+ cells were then analyzed for the expression of CCR7 and CD45RO to identify central memory (CCR7+CD45RO+), effector memory (CCR7-CD45RO+), naïve (CCR7+CD45RO-) and terminally differentiated effector memory (CCR7-CD45RO-) T-cell subsets. The percentage of each T-cell subset was quantified and compared between experimental groups.

Cyclic immunofluorescence staining of tumor microtissues

Microtissue preparation

Vascularized and avascular tumor microtissues were initially fixed with 4% PFA, followed by washing with 1X Dulbecco's Phosphate-Buffered Saline (DPBS). Using a biopsy punch, the microtissues were punched out of the device and then placed into cryomolds containing OCT tissue freezing medium. Microtissues were snap-frozen using dry ice immersed in isopentane (2-methylbutane). Tissue cryosections were loaded onto glass slides and inserted into MACSwell sample carriers to enable immersion in antibody cocktails. Iterative staining using fluorescein isothiocyanate (FITC), phycoerythrin (PE), and allophycocyanin (APC) conjugated antibodies was performed, followed by washing during each image acquisition cycle.

Data analysis

Image acquisition and processing were performed using the MACS iQView. An ROI was drawn to identify the tumor region prior to performing the analysis. DAPI-stained nuclei were segmented using the software's predefined Advanced Tissue Morphology with donut algorithm and validated using visual inspection. This was followed by extraction of cellular phenotypes and related features. Data were imported into GraphPad Prism for statistical analysis.

NanoString GeoMx® Digital Spatial Profiler (DSP)

Microtissue preparation

TCR+T-cell treated HepG2 tumors with or without vasculature were used for NanoString DSP. Glass slides with paraffin-embedded sections were sent to NanoString (Seattle, WA, USA) to perform DSP using the GeoMx Cancer Transcriptome Atlas (CTA) panel. RNA expression of over 1800 genes can be simultaneously analyzed with spatial resolution to characterize tumor biology, TME, and immune responses. Samples were stained with panels of pre-mixed biological probes (each incorporating a unique UV-cleavable DNA barcode) and fluorescently labeled antibodies to visually and differentiate the tumor region (Pan-CK+), endothelial cells (CD31+), and immune cells (CD45+). Regions of interest (ROIs) were chosen within the tumors ("tumor only" and "tumor with vasculature") or in the vasculature region ("ECM") for high-resolution multiplex profiling. Following hybridization, samples were loaded onto an automated nCounter Prep Station (NanoString Technologies) for processing and transfer to nCounter cartridges. These cartridges were then placed in the nCounter Digital Analyzer for imaging and digital counting of individual RNA transcripts. The resulting count data were exported for downstream analysis.

Data processing and analysis

All data were analysed using GeoMx data analysis suite. Quality control (QC) was performed to remove low performing or negative probes. Following data filtering, we calculated the geometric mean for each target within each ROI. The limit of quantification (LOQ) was determine for each ROI, defined as two standard deviations above the geometric mean of negative control probe counts, as is standard in NanoString workflow. If the measurements from target genes within the analysis pipeline exceeded LOQ, those genes were excluded. After filtering 1410 genes remained in the original data set. Statistical tests were applied to determine on geometric means of probe expression to compare the differentially expressed genes between two groups – (1) within the vascularised tumor vs its surrounding ECM region and (2) avascular vs vascularized tumor. Gene set enrichment analysis (GSEA) is implemented using pathway groups from the Reactome database, used by the GeoMx DSP software.

Statistics

All statistical analyses were performed using GraphPad Prism, and the appropriate tests are stated in the figure legends.

Acknowledgments

This work was supported by: i) Open Fund - Young Individual Research Grant (OF-YIRG) - OFYIRG18nov-0002 awarded to AP and GA ii) the Institute of Molecular and Cell Biology, Agency for Science Technology and Research (A*STAR), iii) the Singapore Immunology Network, Agency for Science Technology and Research (A*STAR), and iv) the Mechanobiology Institute, National University of Singapore.

Competing Interest Statement

A.P. is a member of the scientific advisory board and equity holder of AIM Biotech Pte. The other authors declare no competing interests.

References

[1] M. Arnold, C.C. Abnet, R.E. Neale, J. Vignat, E.L. Giovannucci, K.A. McGlynn, F. Bray, Global burden of 5 major types of gastrointestinal cancer, Gastroenterology 159(1) (2020) 335-349. e15.

[2] L.C. Connell, J.J. Harding, J. Shia, G.K. Abou-Alfa, Combined intrahepatic cholangiocarcinoma and hepatocellular carcinoma, Chin Clin Oncol 5(5) (2016) 66.

[3] A. Doyle, A. Gorgen, H. Muaddi, A.D. Aravinthan, A. Issachar, O. Mironov, W. Zhang, J. Kachura, R. Beecroft, S.P. Cleary, Outcomes of radiofrequency ablation as first-line therapy for hepatocellular carcinoma less than 3 cm in potentially transplantable patients, Journal of hepatology 70(5) (2019) 866-873.

[4] J.M. Llovet, S. Ricci, V. Mazzaferro, P. Hilgard, E. Gane, J.-F. Blanc, A.C. De Oliveira, A. Santoro, J.-L. Raoul, A. Forner, Sorafenib in advanced hepatocellular carcinoma, New England journal of medicine 359(4) (2008) 378-390.

[5] M. Kudo, R.S. Finn, S. Qin, K.-H. Han, K. Ikeda, F. Piscaglia, A. Baron, J.-W. Park, G. Han, J. Jassem, Lenvatinib versus sorafenib in first-line treatment of patients with unresectable hepatocellular carcinoma: a randomised phase 3 non-inferiority trial, The Lancet 391(10126) (2018) 1163-1173.

[6] J. Bruix, S. Qin, P. Merle, A. Granito, Y.-H. Huang, G. Bodoky, M. Pracht, O. Yokosuka, O. Rosmorduc, V. Breder, Regorafenib for patients with hepatocellular carcinoma who progressed on sorafenib treatment (RESORCE): a randomised, double-blind, placebo-controlled, phase 3 trial, The Lancet 389(10064) (2017) 56-66.

[7] G.K. Abou-Alfa, T. Meyer, A.-L. Cheng, A.B. El-Khoueiry, L. Rimassa, B.-Y. Ryoo, I. Cicin, P. Merle, Y. Chen, J.-W. Park, Cabozantinib in patients with advanced and progressing hepatocellular carcinoma, New England Journal of Medicine 379(1) (2018) 54-63.

[8] Y.-J. Zhu, B. Zheng, H.-Y. Wang, L. Chen, New knowledge of the mechanisms of sorafenib resistance in liver cancer, Acta Pharmacologica Sinica 38(5) (2017) 614-622.

[9] H. Jin, Y. Shi, Y. Lv, S. Yuan, C.F. Ramirez, C. Lieftink, L. Wang, S. Wang, C. Wang, M.H. Dias, EGFR activation limits the response of liver cancer to lenvatinib, Nature 595(7869) (2021) 730-734.

[10] H. Dai, C. Tong, D. Shi, M. Chen, Y. Guo, D. Chen, X. Han, H. Wang, Y. Wang, P. Shen, Efficacy and biomarker analysis of CD133-directed CAR T cells in advanced hepatocellular carcinoma: a single-arm, open-label, phase II trial, Oncoimmunology 9(1) (2020) 1846926.

[11] H. Sun, C. Xing, S. Jiang, K. Yu, S. Dai, H. Kong, Y. Jin, Y. Shan, W. Yang, Z. Wang, Long term complete response of advanced hepatocellular carcinoma to glypican-3 specific chimeric antigen receptor T-Cells plus sorafenib, a case report, Frontiers in Immunology 13 (2022) 963031.

[12] A.T. Tan, F. Meng, J. Jin, J.Y. Zhang, S.Y. Wang, L. Shi, M. Shi, Y. Li, Y. Xie, L.M. Liu, Immunological alterations after immunotherapy with short lived HBV-TCR T cells associates with long-term treatment response in HBV-HCC, Hepatology Communications 6(4) (2022) 841-854.

[13] F. Meng, J. Zhao, A.T. Tan, W. Hu, S.-Y. Wang, J. Jin, J. Wu, Y. Li, L. Shi, J.-L. Fu, Immunotherapy of HBV-related advanced hepatocellular carcinoma with short-term HBV-specific TCR expressed T cells: results of dose escalation, phase I trial, Hepatology International 15 (2021) 1402-1412.

[14] T. Sükei, E. Palma, L. Urbani, Interplay between cellular and non-cellular components of the tumour microenvironment in hepatocellular carcinoma, Cancers 13(21) (2021) 5586.

[15] R. Abou Khouzam, K. Brodaczewska, A. Filipiak, N.A. Zeinelabdin, S. Buart, C. Szczylik, C. Kieda, S. Chouaib, Tumor hypoxia regulates immune escape/invasion: influence on angiogenesis and potential impact of hypoxic biomarkers on cancer therapies, Frontiers in Immunology 11 (2021) 613114.

[16] F. Mpekris, C. Voutouri, J.W. Baish, D.G. Duda, L.L. Munn, T. Stylianopoulos, R.K. Jain, Combining microenvironment normalization strategies to improve cancer immunotherapy, Proceedings of the National Academy of Sciences 117(7) (2020) 3728-3737.

[17] C.P. Camargo, A.K. Muhuri, Y. Alapan, L.F. Sestito, M. Khosla, M.P. Manspeaker, A.S. Smith, C.M. Paulos, S.N. Thomas, Adhesion analysis via a tumor vasculature-like microfluidic device identifies CD8+ T cells with enhanced tumor homing to improve cell therapy, Cell reports 42(3) (2023).

[18] A.N. Woods, A.L. Wilson, N. Srivinisan, J. Zeng, A.B. Dutta, J.D. Peske, E.F. Tewalt, R.K. Gregg, A.R. Ferguson, V.H. Engelhard, Differential expression of homing receptor ligands on tumor-associated vasculature that control CD8 effector T-cell entry, Cancer immunology research 5(12) (2017) 1062-1073.

[19] J. Rodrigues, M.A. Heinrich, L.M. Teixeira, J. Prakash, 3D in vitro model (R) evolution: unveiling tumor–stroma interactions, Trends in cancer 7(3) (2021) 249-264.

[20] M. Lam, J. Reales-Calderon, J.R. Ow, A. Joey, T. Damien, E. Ceccarello, T. TABAGLIO, Y.T. Lim, L.C. Wang, R. Sobota, G9a/GLP inhibition during ex vivo lymphocyte expansion increases in vivo cytotoxicity of engineered TCR-T cells against hepatocellular carcinoma, (2021).

[21] J.M. Ayuso, S. Rehman, M. Virumbrales-Munoz, P.H. McMinn, P. Geiger, C. Fitzgerald, T. Heaster, M.C. Skala, D.J. Beebe, Microfluidic tumor-on-a-chip model to evaluate the role of tumor environmental stress on NK cell exhaustion, Science Advances 7(8) (2021) eabc2331.

[22] M.S. Lam, J.J. Aw, D. Tan, R. Vijayakumar, H.Y.G. Lim, S. Yada, Q.Y. Pang, N. Barker, C. Tang, B.T. Ang, Unveiling the Influence of Tumor Microenvironment and Spatial Heterogeneity on Temozolomide Resistance in Glioblastoma Using an Advanced Human In Vitro Model of the Blood-Brain Barrier and Glioblastoma, Small (2023) 2302280.

[23] G. Adriani, A. Pavesi, The OrganiX microfluidic system to recreate the complex tumour microenvironment, Nature Reviews Immunology (2024) 1-1.

[24] J. Ahn, D.-H. Kim, D.-J. Koo, J. Lim, T.-E. Park, J. Lee, J. Ko, S. Kim, M. Kim, K.-S. Kang, D.-H. Min, S.-Y. Kim, Y. Kim, N.L. Jeon, 3D microengineered vascularized tumor spheroids for drug delivery and efficacy testing, Acta Biomaterialia 165 (2023) 153-167.

[25] Y. Nashimoto, R. Okada, S. Hanada, Y. Arima, K. Nishiyama, T. Miura, R. Yokokawa, Vascularized cancer on a chip: The effect of perfusion on growth and drug delivery of tumor spheroid, Biomaterials 229 (2020) 119547.

[26] J. Ko, S. Hyung, Y.J. Heo, S. Jung, S.T. Kim, S.H. Park, J.Y. Hong, S.H. Lim, K.-M. Kim, S. Yoo, Patient-derived tumor spheroid-induced angiogenesis preclinical platform for exploring therapeutic vulnerabilities in cancer, Biomaterials (2024) 122504.

[27] Y. Bi, V.S. Shirure, R. Liu, C. Cunningham, L. Ding, J.M. Meacham, S.P. Goedegebuure, S.C. George, R.C. Fields, Tumor-on-a-chip platform to interrogate the role of macrophages in tumor progression, Integr Biol (Camb) 12(9) (2020) 221-232.

[28] A. Boussommier-Calleja, Y. Atiyas, K. Haase, M. Headley, C. Lewis, R.D. Kamm, The effects of monocytes on tumor cell extravasation in a 3D vascularized microfluidic model, Biomaterials 198 (2019) 180-193.

[29] M.B. Chen, C. Hajal, D.C. Benjamin, C. Yu, H. Azizgolshani, R.O. Hynes, R.D. Kamm, Inflamed neutrophils sequestered at entrapped tumor cells via chemotactic confinement promote tumor cell extravasation, Proceedings of the National Academy of Sciences 115(27) (2018) 7022-7027.

[30] H. Mollica, Y.J. Teo, A.S.M. Tan, D.Z.M. Tan, P. Decuzzi, A. Pavesi, G. Adriani, A 3D pancreatic tumor model to study T cell infiltration, Biomaterials Science 9(22) (2021) 7420-7431.

[31] Z. Wan, M.A. Floryan, M.F. Coughlin, S. Zhang, A.X. Zhong, S.E. Shelton, X. Wang, C. Xu, D.A. Barbie, R.D. Kamm, New strategy for promoting vascularization in tumor spheroids in a microfluidic assay, Advanced healthcare materials 12(14) (2023) 2201784.

[32] Y. Wang, M. Chen, Z. Wu, C. Tong, H. Dai, Y. Guo, Y. Liu, J. Huang, H. Lv, C. Luo, K.C. Feng, Q.M. Yang, X.L. Li, W. Han, CD133-directed CAR T cells for advanced metastasis malignancies: A phase I trial, Oncoimmunology 7(7) (2018) e1440169.

[33] A.-L. Cheng, Y.-K. Kang, Z. Chen, C.-J. Tsao, S. Qin, J.S. Kim, R. Luo, J. Feng, S. Ye, T.-S. Yang, Efficacy and safety of sorafenib in patients in the Asia-Pacific region with advanced hepatocellular carcinoma: a phase III randomised, double-blind, placebo-controlled trial, The lancet oncology 10(1) (2009) 25-34.

[34] S. Yang, G. Liu, Targeting the Ras/Raf/MEK/ERK pathway in hepatocellular carcinoma, Oncology letters 13(3) (2017) 1041-1047.

[35] M. Xu, Y.-l. Zheng, X.-y. Xie, J.-y. Liang, F.-s. Pan, S.-g. Zheng, M.-d. Lü, Sorafenib blocks the HIF-1α/VEGFA pathway, inhibits tumor invasion, and induces apoptosis in hepatoma cells, DNA and Cell Biology 33(5) (2014) 275-281.

[36] S.S. Lee-Sayer, N. Maeshima, M.N. Dougan, A. Dahiya, A.A. Arif, M. Dosanjh, C.A. Maxwell, P. Johnson, Hyaluronan-binding by CD44 reduces the memory potential of activated murine CD8 T cells, European Journal of Immunology 48(5) (2018) 803-814.

[37] R. Tinoco, D.C. Otero, A.A. Takahashi, L.M. Bradley, PSGL-1: a new player in the immune checkpoint landscape, Trends in immunology 38(5) (2017) 323-335.

[38] H.-P. Ma, H.-L. Chang, O.A. Bamodu, V.K. Yadav, T.-Y. Huang, A.T. Wu, C.-T. Yeh, S.-H. Tsai, W.-H. Lee, Collagen 1A1 (COL1A1) is a reliable biomarker and putative therapeutic target for hepatocellular carcinogenesis and metastasis, Cancers 11(6) (2019) 786.

[39] C. Lee, M. Kim, J.H. Lee, J. Oh, H.H. Shin, S.M. Lee, P.E. Scherer, H.M. Kwon, J.H. Choi, J. Park, COL6A3-derived endotrophin links reciprocal interactions among hepatic cells in the pathology of chronic liver disease, The Journal of pathology 247(1) (2019) 99-109.

[40] Y. Lu, Z. Fang, M. Li, Q. Chen, T. Zeng, L. Lu, Q. Chen, H. Zhang, Q. Zhou, Y. Sun, Dynamic edge-based biomarker non-invasively predicts hepatocellular carcinoma with hepatitis B virus infection for individual patients based on blood testing, Journal of Molecular Cell Biology 11(8) (2019) 665-677.

[41] Z. Song, X. Wang, X. Liu, Y. Luo, J. Qiu, A. Yin, Y. Liu, H. Yi, Z. Xiao, A. Li, Targeting of Annexin A1 in Tumor-associated Macrophages as a therapeutic strategy for hepatocellular carcinoma, Biochemical Pharmacology 213 (2023) 115612.

[42] L. Zhao, D. He, M. Jiao, L. Kong, C. Shao, J. Chen, Z. Fang, X. Ma, H. Chen, L. Li, Overexpression of histone deacetylase and amyloid precursor protein in hepatocellular carcinoma, Technology in cancer research & treatment 16(5) (2017) 586-594.

[43] Y. Luo, Y. Tan, Prognostic value of CD44 expression in patients with hepatocellular carcinoma: meta-analysis, Cancer cell international 16(1) (2016) 1-9.

[44] Y. Li, S. Yu, L. Li, J. Chen, M. Quan, Q. Li, Y. Gao, KLF4-mediated upregulation of CD9 and CD81 suppresses hepatocellular carcinoma development via JNK signaling, Cell death & disease 11(4) (2020) 299.

[45] D.-H. Kim, J. Ahn, H.K. Kang, M.-S. Kim, N.-G. Kim, M.G. Kook, S.W. Choi, N.L. Jeon, H.-M. Woo, K.-S. Kang, Development of highly functional bioengineered human liver with perfusable vasculature, Biomaterials 265 (2021) 120417.

[46] R.T. Poon, K.K. Chung, S.T. Cheung, C.P. Lau, S.W. Tong, K.L. Leung, W.C. Yu, G.P. Tuszynski, S.T. Fan, Clinical significance of thrombospondin 1 expression in hepatocellular carcinoma, Clin Cancer Res 10(12 Pt 1) (2004) 4150-7.

[47] Y. Li, C.P. Turpin, S. Wang, Role of thrombospondin 1 in liver diseases, Hepatol Res 47(2) (2017) 186-193.

[48] Y. Tang, X. Yang, K. Feng, C. Hu, S. Li, High expression of aldolase A is associated with tumor progression and poor prognosis in hepatocellular carcinoma, Journal of Gastrointestinal Oncology 12(1) (2021) 174.

[49] M. Uhlen, C. Zhang, S. Lee, E. Sjöstedt, L. Fagerberg, G. Bidkhori, R. Benfeitas, M. Arif, Z. Liu, F. Edfors, A pathology atlas of the human cancer transcriptome, Science 357(6352) (2017) eaan2507.

[50] Y. Niu, Z. Lin, A. Wan, L. Sun, S. Yan, H. Liang, S. Zhan, D. Chen, X. Bu, P. Liu, Loss-of-function genetic screening identifies aldolase a as an essential driver for liver cancer cell growth under hypoxia, Hepatology 74(3) (2021) 1461-1479.

[51] E. Horwitz, I. Stein, M. Andreozzi, J. Nemeth, A. Shoham, O. Pappo, N. Schweitzer, L. Tornillo, N. Kanarek, L. Quagliata, Human and mouse VEGFA-amplified hepatocellular carcinomas are highly sensitive to sorafenib treatment, Cancer discovery 4(6) (2014) 730-743.

[52] N. Pavlović, F. Heindryckx, Exploring the role of endoplasmic reticulum stress in hepatocellular carcinoma through mining of the human protein atlas, Biology 10(7) (2021) 640.

[53] H. Guo, J. Zhou, Y. Zhang, Z. Wang, L. Liu, W. Zhang, Identification of hypoxia-related differentially expressed genes and construction of the clinical prognostic predictor in hepatocellular carcinoma by bioinformatic analysis, BioMed Research International 2021 (2021) 1-15.

[54] L. Duan, R. Wu, X. Zhang, D. Wang, Y. You, Y. Zhang, L. Zhou, W. Chen, HBx-induced S100A9 in NF-κB dependent manner promotes growth and metastasis of hepatocellular carcinoma cells, Cell death & disease 9(6) (2018) 629.

[55] W. Sun, J. Shen, J. Liu, K. Han, L. Liang, Y. Gao, Gene signature and prognostic value of ubiquitin-specific proteases members in hepatocellular carcinoma and explored the immunological role of Usp36, Frontiers in Bioscience-Landmark 27(6) (2022) 190.

[56] C. Guo, Y. Ouyang, J. Cai, L. Xiong, Y. Chen, X. Zeng, A. Liu, High expression of IL-4R enhances proliferation and invasion of hepatocellular carcinoma cells, The International Journal of Biological Markers 32(4) (2017) 384-390.

[57] K.-J. Chen, S.-Z. Lin, L. Zhou, H.-Y. Xie, W.-H. Zhou, A. Taki-Eldin, S.-S. Zheng, Selective recruitment of regulatory T cell through CCR6-CCL20 in hepatocellular carcinoma fosters tumor progression and predicts poor prognosis, PloS one 6(9) (2011) e24671.

[58] L. Zhao, Y. Jin, C. Yang, C. Li, HBV-specific CD8 T cells present higher TNF-α expression but lower cytotoxicity in hepatocellular carcinoma, Clinical & Experimental Immunology 201(3) (2020) 289-296.

[59] P. Dietrich, A. Koch, V. Fritz, A. Hartmann, A.K. Bosserhoff, C. Hellerbrand, Wild type Kirsten rat sarcoma is a novel microRNA-622-regulated therapeutic target for hepatocellular carcinoma and contributes to sorafenib resistance, Gut 67(7) (2018) 1328-1341.

[60] X. Yin, B. Tang, J.-H. Li, Y. Wang, L. Zhang, X.-Y. Xie, B.-H. Zhang, S.-J. Qiu, W.-Z. Wu, Z.-G. Ren, ID1 promotes hepatocellular carcinoma proliferation and confers chemoresistance to oxaliplatin by activating pentose phosphate pathway, Journal of Experimental & Clinical Cancer Research 36(1) (2017) 1-13.

[61] E. Sano, C. Mori, Y. Nashimoto, R. Yokokawa, H. Kotera, Y.-s. Torisawa, Engineering of vascularized 3D cell constructs to model cellular interactions through a vascular network, Biomicrofluidics 12(4) (2018).

[62] M. Campisi, S.K. Sundararaman, S.E. Shelton, E.H. Knelson, N.R. Mahadevan, R. Yoshida, T. Tani, E. Ivanova, I. Cañadas, T. Osaki, Tumor-derived cGAMP regulates activation of the vasculature, Frontiers in Immunology 11 (2020) 2090.

[63] S. Lee, S. Kim, D.-J. Koo, J. Yu, H. Cho, H. Lee, J.M. Song, S.-Y. Kim, D.-H. Min, N.L. Jeon, 3D microfluidic platform and tumor vascular mapping for evaluating anti-angiogenic RNAi-based nanomedicine, ACS nano 15(1) (2020) 338-350.

[64] C. Quintard, E. Tubbs, G. Jonsson, J. Jiao, J. Wang, N. Werschler, C. Laporte, A. Pitaval, T.-S. Bah, G. Pomeranz, A microfluidic platform integrating functional vascularized organoids-on-chip, Nature Communications 15(1) (2024) 1452.

[65] T. Petreus, E. Cadogan, G. Hughes, A. Smith, V. Pilla Reddy, A. Lau, M.J. O'Connor, S. Critchlow, M. Ashford, L. Oplustil O'Connor, Tumour-on-chip microfluidic platform for assessment of drug pharmacokinetics and treatment response, Communications Biology 4(1) (2021) 1001.

[66] S. Däster, N. Amatruda, D. Calabrese, R. Ivanek, E. Turrini, R.A. Droeser, P. Zajac, C. Fimognari, G.C. Spagnoli, G. Iezzi, V. Mele, M.G. Muraro, Induction of hypoxia and necrosis in multicellular tumor spheroids is associated with resistance to chemotherapy treatment, Oncotarget 8(1) (2016).

[67] J. He, C. Zhou, X. Xu, Z. Zhou, M. Danoy, M. Shinohara, W. Xiao, D. Zhu, X. Zhao, X. Feng, Scalable Formation of Highly Viable and Functional Hepatocellular Carcinoma Spheroids in an Oxygen-Permeable Microwell Device for Anti-Tumor Drug Evaluation, Advanced Healthcare Materials 11(18) (2022) 2200863.

[68] M.R. Dreher, W. Liu, C.R. Michelich, M.W. Dewhirst, F. Yuan, A. Chilkoti, Tumor vascular permeability, accumulation, and penetration of macromolecular drug carriers, Journal of the National Cancer Institute 98(5) (2006) 335-344.

[69] E.B. Brown, R.B. Campbell, Y. Tsuzuki, L. Xu, P. Carmeliet, D. Fukumura, R.K. Jain, In vivo measurement of gene expression, angiogenesis and physiological function in tumors using multiphoton laser scanning microscopy, Nature medicine 7(7) (2001) 864-868.

[70] G.H. Qiu, X. Xie, F. Xu, X. Shi, Y. Wang, L. Deng, Distinctive pharmacological differences between liver cancer cell lines HepG2 and Hep3B, Cytotechnology 67(1) (2015) 1-12.

[71] M. Lam, J.A. Reales-Calderon, J.R. Ow, G. Adriani, A. Pavesi, In vitro 3D liver tumor microenvironment models for immune cell therapy optimization, APL bioengineering 5(4) (2021).

[72] R. Lugano, M. Ramachandran, A. Dimberg, Tumor angiogenesis: causes, consequences, challenges and opportunities, Cellular and Molecular Life Sciences 77 (2020) 1745-1770.

[73] Z.-L. Liu, H.-H. Chen, L.-L. Zheng, L.-P. Sun, L. Shi, Angiogenic signaling pathways and anti-angiogenic therapy for cancer, Signal transduction and targeted therapy 8(1) (2023) 198.

[74] R. Zhang, Y. Yao, H. Gao, X. Hu, Mechanisms of angiogenesis in tumour, Frontiers in Oncology 14 (2024) 1359069.

[75] K. Kane, D. Edwards, J. Chen, The influence of endothelial metabolic reprogramming on the tumor microenvironment, Oncogene (2024) 1-13.

[76] Y. Yang, G. Zhang, F. Guo, Q. Li, H. Luo, Y. Shu, Y. Shen, J. Gan, L. Xu, H. Yang, Mitochondrial UQCC3 modulates hypoxia adaptation by orchestrating OXPHOS and glycolysis in hepatocellular carcinoma, Cell Reports 33(5) (2020).

[77] Z. Mo, D. Liu, D. Rong, S. Zhang, Hypoxic characteristic in the immunosuppressive microenvironment of hepatocellular carcinoma, Frontiers in immunology 12 (2021) 611058.

[78] H. Li, Angiogenesis in the progression from liver fibrosis to cirrhosis and hepatocelluar carcinoma, Expert review of gastroenterology & hepatology 15(3) (2021) 217-233.

[79] M. Bouattour, N. Mehta, A.R. He, E.I. Cohen, J.-C. Nault, Systemic treatment for advanced hepatocellular carcinoma, Liver cancer 8(5) (2019) 341-358.

[80] W. He, L. Liao, D. Hu, B. Li, C. Wang, J. Qiu, Y. Liao, W. Liu, Z. Yang, Y. Zhang, Apatinib versus sorafenib in patients with advanced hepatocellular carcinoma: a preliminary study, Annals of Translational Medicine 8(16) (2020).

[81] J. Rimola, Á. Díaz-González, A. Darnell, M. Varela, F. Pons, M. Hernandez-Guerra, M. Delgado, J. Castroagudin, A. Matilla, B. Sangro, Complete response under sorafenib in patients with hepatocellular carcinoma: Relationship with dermatologic adverse events, Hepatology 67(2) (2018) 612-622.

[82] J. Luo, B. Gao, Z. Lin, H. Fan, W. Ma, D. Yu, Q. Yang, J. Tian, X. Yang, B. Li, Efficacy and safety of lenvatinib versus sorafenib in first-line treatment of advanced hepatocellular carcinoma: A meta-analysis, Frontiers in Oncology 12 (2022) 1010726.

[83] A. Runge, J. Hu, M. Wieland, J.-P. Bergeest, C. Mogler, A. Neumann, C. Géraud, B. Arnold, K. Rohr, D. Komljenovic, An inducible hepatocellular carcinoma model for preclinical evaluation of antiangiogenic therapy in adult mice, Cancer research 74(15) (2014) 4157-4169.

[84] M. Kissel, S. Berndt, L. Fiebig, S. Kling, Q. Ji, Q. Gu, T. Lang, F.-T. Hafner, M. Teufel, D. Zopf, Antitumor effects of regorafenib and sorafenib in preclinical models of hepatocellular carcinoma, Oncotarget 8(63) (2017) 107096.

[85] G.-H. Qiu, X. Xie, F. Xu, X. Shi, Y. Wang, L. Deng, Distinctive pharmacological differences between liver cancer cell lines HepG2 and Hep3B, Cytotechnology 67 (2015) 1-12.

[86] S.-C. Lai, Y.-T. Su, C.-C. Chi, Y.-C. Kuo, K.-F. Lee, Y.-C. Wu, P.-C. Lan, M.-H. Yang, T.-S. Chang, Y.-H. Huang, DNMT3b/OCT4 expression confers sorafenib resistance and poor prognosis of hepatocellular carcinoma through IL-6/STAT3 regulation, Journal of Experimental & Clinical Cancer Research 38 (2019) 1-18.

[87] D.C. Kahraman, T. Kahraman, R. Cetin-Atalay, Targeting PI3K/Akt/mTOR pathway identifies differential expression and functional role of IL8 in liver cancer stem cell enrichment, Molecular cancer therapeutics 18(11) (2019) 2146-2157.

[88] O. Öcal, K. Schütte, J. Kupčinskas, E. Morkunas, G. Jurkeviciute, E.N. de Toni, N. Ben Khaled, T. Berg, P. Malfertheiner, H.J. Klümpen, Baseline Interleukin-6 and-8 predict response and survival in patients with advanced hepatocellular carcinoma treated with sorafenib monotherapy: an exploratory post hoc analysis of the SORAMIC trial, Journal of cancer research and clinical oncology (2022) 1-11.

[89] C. Yang, J. You, Q. Pan, Y. Tang, L. Cai, Y. Huang, J. Gu, Y. Wang, X. Yang, Y. Du, Targeted delivery of a PD-1-blocking scFv by CD133-specific CAR-T cells using nonviral Sleeping Beauty transposition shows enhanced antitumour efficacy for advanced hepatocellular carcinoma, BMC medicine 21(1) (2023) 327.

[90] Y. Wang, M. Chen, Z. Wu, C. Tong, H. Dai, Y. Guo, Y. Liu, J. Huang, H. Lv, C. Luo, CD133-directed CAR T cells for advanced metastasis malignancies: A phase I trial, Oncoimmunology 7(7) (2018) e1440169.

[91] P. Xu, J. Chi, X. Wang, M. Zhu, K. Chen, Q. Fan, F. Ye, C. Shao, In vitro vascularized liver tumor model based on a microfluidic inverse opal scaffold for immune cell recruitment investigation, Lab on a Chip (2024).

[92] D. Teng, L. Ding, B. Cai, Q. Luo, H. Wang, Interleukin-7 enhances anti-tumor activity of CD8+ T cells in patients with hepatocellular carcinoma, Cytokine 118 (2019) 115-123.

[93] Y. Yan, L. Zheng, Q. Du, H. Yazdani, K. Dong, Y. Guo, D.A. Geller, Interferon regulatory factor 1 (IRF-1) activates anti-tumor immunity via CXCL10/CXCR3 axis in hepatocellular carcinoma (HCC), Cancer letters 506 (2021) 95-106.

[94] A. Makkouk, X.C. Yang, T. Barca, A. Lucas, M. Turkoz, J.T. Wong, K.P. Nishimoto, M.M. Brodey, M. Tabrizizad, S.R. Gundurao, Off-the-shelf Vδ1 gamma delta T cells engineered with glypican-3 (GPC-3)-specific chimeric antigen receptor (CAR) and soluble IL-15 display robust antitumor efficacy against hepatocellular carcinoma, Journal for immunotherapy of cancer 9(12) (2021).

[95] Y. Zhang, X.-y. Guan, P. Jiang, Cytokine and chemokine signals of T-cell exclusion in tumors, Frontiers in immunology 11 (2020) 594609.

[96] K. Shigeta, A. Matsui, H. Kikuchi, S. Klein, E. Mamessier, I.X. Chen, S. Aoki, S. Kitahara, K. Inoue, A. Shigeta, Regorafenib combined with PD1 blockade increases CD8 T-cell infiltration by inducing CXCL10 expression in hepatocellular carcinoma, Journal for immunotherapy of cancer 8(2) (2020).

[97] L.-X. Yu, Y. Ling, H.-Y. Wang, Role of nonresolving inflammation in hepatocellular carcinoma development and progression, NPJ precision oncology 2(1) (2018) 6.

[98] B.P. Keenan, L. Fong, R.K. Kelley, Immunotherapy in hepatocellular carcinoma: the complex interface between inflammation, fibrosis, and the immune response, Journal for immunotherapy of cancer 7 (2019) 1-13.

[99] Y. Lin, S. Huang, Y. Qi, L. Xie, J. Jiang, H. Li, Z. Chen, PSGL-1 is a novel tumor microenvironment prognostic biomarker with cervical high-grade squamous lesions and more, Frontiers in Oncology 13 (2023) 1052201.

[100] J.L. Hope, D.C. Otero, E.-A. Bae, C.J. Stairiker, A.B. Palete, H.A. Faso, M. Lin, M.L. Henriquez, S. Roy, H. Seo, PSGL-1 attenuates early TCR signaling to suppress CD8+ T cell progenitor differentiation and elicit terminal CD8+ T cell exhaustion, Cell reports 42(5) (2023).

[101] J.M. DeRogatis, K.M. Viramontes, E.N. Neubert, M.L. Henriquez, C.F. Guerrero-Juarez, R. Tinoco, Targeting the PSGL-1 Immune Checkpoint Promotes Immunity to PD-1–Resistant Melanoma, Cancer immunology research 10(5) (2022) 612-625.

[102] T.H. Schreiber, E.R. Podack, Immunobiology of TNFSF15 and TNFRSF25, Immunologic research 57 (2013) 3-11.

[103] T.J. Slebioda, T.F. Rowley, J.R. Ferdinand, J.E. Willoughby, S.L. Buchan, V.Y. Taraban, A. Al-Shamkhani, Triggering of TNFRSF25 promotes CD8+ T-cell responses and anti-tumor immunity, European Journal of Immunology 41(9) (2011) 2606-2611.

[104] G.S. Offeddu, L. Possenti, J.T. Loessberg-Zahl, P. Zunino, J. Roberts, X. Han, D. Hickman, C.G. Knutson, R.D. Kamm, Application of Transmural Flow Across In Vitro Microvasculature Enables Direct Sampling of Interstitial Therapeutic Molecule Distribution, Small 15(46) (2019) e1902393.

Highlights

- Developed an *in vitro* model of a human liver tumor integrated with a functional vasculature within a microfluidic platform
- Sorafenib disrupted tumor vasculature and induced heterogenous responses in different liver tumor subtypes
- Tumor vasculature reduced the infiltration of engineered T-cells but preserved its cytotoxic capacity
- Spatial profiling of the tumor microenvironment revealed activation and exhaustion patterns in engineered T-cells

Declaration of interests

☐ The authors declare that they have no known competing financial interests or personal relationships that could have appeared to influence the work reported in this paper.

☒ The authors declare the following financial interests/personal relationships which may be considered as potential competing interests:

Andrea Pavesi reports a relationship with AIM Biotech pte ltd that includes: board membership and equity or stocks. Andrea Pavesi has patent licensed to Aim biotech. Giulia Adriani has patent licensed to Aim biotech. If there are other authors, they declare that they have no known competing financial interests or personal relationships that could have appeared to influence the work reported in this paper.